






Ferrofluid droplets in planar extensional flows: Droplet shape and magnetization reveal novel rheological signatures of ferrofluid emulsions

A. L. Guilherme ¹, I. R. Siqueira ^{2,*}, L. H. P. Cunha ^{2,3,*}
R. L. Thompson ⁴ and T. F. Oliveira ^{1,†}

¹*Department of Mechanical Engineering, Universidade de Brasília, Brasília, DF 70910-900, Brazil*

²*Department of Chemical and Biomolecular Engineering, Rice University, Houston, Texas 77005, United States*

³*Center for Theoretical Biological Physics, Rice University, Houston, Texas 77005, United States*

⁴*Department of Mechanical Engineering, Universidade Federal do Rio de Janeiro, Rio de Janeiro, RJ 21941-972, Brazil*



(Received 20 December 2022; accepted 1 May 2023; published 2 June 2023)

We present a three-dimensional computational study of the impact of external magnetic fields on the dynamics of superparamagnetic ferrofluid droplets and rheology of dilute ferrofluid emulsions in planar extensional flows. Specifically, we show how the intensity and direction of uniform magnetic fields affect the planar extensional rheology of ferrofluid emulsions by changing the shape and magnetization of the constituent ferrofluid droplets in suspension. We find that the two traditional extensional viscosities associated with the normal stresses of the bulk emulsion in extension either remain constant or increase with the field intensity; the only exception occurs when the field direction is perpendicular to the extension plane, where increasing the field intensity keeps the planar extensional viscosity constant and modestly decreases the second extensional viscosity. We also find that the droplet tilts in the flow when the external field is not aligned with one of the flow main directions, which changes the recirculation pattern and flow topology inside the droplet. At the microscopic level, the droplet experiences a magnetic torque because of a small misalignment between its magnetization and the external field direction. At the macroscopic level, the bulk emulsion experiences a field-induced internal torque that leads to a nonsymmetric stress tensor with unexpected shear components in extension. To account for this unconventional stress-strain response, we introduce new extensional material functions such as shear and rotational viscosity coefficients that unveil novel rheological signatures of ferrofluid emulsions in planar extensional flows. This study offers new insights into applications based on the field-assisted manipulation of ferrofluid droplets and sheds light on the potential of ferrofluid emulsions as a model system for chiral fluids with internal rotational degrees of freedom that can be activated and controlled by coupling static magnetic fields with hydrodynamic flows.

DOI: [10.1103/PhysRevFluids.8.063601](https://doi.org/10.1103/PhysRevFluids.8.063601)

I. INTRODUCTION

Ferrofluids are colloidal suspensions of ferromagnetic nanoparticles that effectively behave like paramagnetic liquids in the presence of magnetic fields [1–3]. Since their formal discovery by Papell [4] in the 1960s, ferrofluids have emerged as a new class of smart materials whose properties

*These authors contributed equally to this work.

†Corresponding author: taygoara@unb.br

and functionality can be remotely controlled by external magnetic fields. The improvement of applications based on ferrofluid droplets over recent years is particularly impressive and merits attention. For instance, the field-assisted manipulation of ferrofluid droplets can play a central role in the development of next-generation microfluidic and lab-on-a-chip technologies [5–8]. Additionally, recent works have demonstrated the potential of ferrofluid droplets as unique building blocks for manufacturing microrheology probes [9–11] and soft robots [12–14]. The reader can find comprehensive discussions on the basic principles and field-mediated applications of ferrofluids and other magnetically responsive colloids in some recently available reviews [15–17].

After decades of fundamental progress, the field-induced distortion, motion, interaction, and coalescence of ferrofluid droplets in an otherwise quiescent liquid are well established [18–29]. Conversely, the dynamics of ferrofluid droplets under the simultaneous action of external magnetic fields and hydrodynamic flows is yet to be fully understood. As far as we are aware, the first study in this regard was presented by Jesus *et al.* [30], who analyzed the behavior of superparamagnetic ferrofluid droplets in simple shear flows when uniform magnetic fields are externally applied in the velocity gradient direction. Based on the classical analysis of Taylor [31,32] for viscous droplets, they developed a small deformation theory for the droplet distortion at the limit of weak flows and low field intensities and presented simulation results for the droplet shape and orientation at different conditions. The work of Jesus *et al.* [30] was quickly followed by a handful of similar studies by different authors [33–38]. Despite differences in formulation and solution method, these studies confirmed that the droplet assumes the format of a general ellipsoid, either prolate- or oblatelike, whose shape and orientation are determined by a delicate balance between viscous, magnetic, and capillary forces that essentially depends on the external field intensity and direction relative to the flow. In a similar fashion, other studies showed that the coupling of flow- and field-induced distortion also plays an important role in the breakup dynamics of ferrofluid droplets in shear flows [39–41]. Recently Ishida *et al.* [42] reported an interesting chain-to-crystal transition in the arrangement of multiple ferrofluid droplets in wall-bounded shear flows, and Abdo *et al.* [43] studied the dynamic response of single ferrofluid droplets in unbounded oscillatory shear flows.

Following the seminal theory of Batchelor [44], single-droplet studies pave the way to predict the rheology of dilute emulsions in which droplet–droplet interactions are negligible. Briefly, the approach relies on the so-called particle stress, a stress tensor that accounts for the additional stresses induced by the suspended droplets in the continuous phase when the two-phase system is taken as a homogeneous rheological material from a continuum perspective [45,46]. For ordinary viscous droplets, the extra stresses arise from the viscosity difference and interfacial tension between the phases. Fundamental studies of the rheology of such emulsions abound [47–52]. In turn, ferrofluid droplets experience an additional field-induced magnetic traction because the magnetic permeability difference between the phases induces a magnetic field discontinuity across the fluid interface. Taking advantage of the level set framework for multiphase flows, Cunha *et al.* [35] introduced a new formulation for the particle stress of ferrofluid droplets in suspension. Shortly after, Ishida and Matsunaga [36] and Capobianchi *et al.* [37] presented similar studies using other interface-capturing methods. These three works addressed the rheology of dilute ferrofluid emulsions in simple shear flows and showed that the traditional viscometric material functions (shear viscosity and normal stress coefficients) can be effectively tuned by external magnetic fields. Recently, Abdo *et al.* [43] extended these analyses to the unsteady material functions (storage and loss moduli) in small-amplitude oscillatory shear flows.

Things become even more interesting when one looks at the droplet magnetization. If the droplet is superparamagnetic and the external field is uniform, the droplet magnetization in a quiescent liquid is uniform and parallel to the external field direction, provided that the field-induced distortion is not sufficiently strong to disrupt the droplet ellipsoidal shape [27]. As first noted by Cunha *et al.* [35], and later detailed by Abicalil *et al.* [38], this is not true for ferrofluid droplets in shear flows. As in a quiescent liquid, the droplet shape remains ellipsoidal if the external field intensity is not too high; yet the competition between viscous, magnetic, and capillary forces, together with the effects of flow vorticity, leads to a small misalignment between the droplet magnetization and the external

field direction. As a result, there is a magnetic torque that tends to tilt the droplet major axis towards the external field direction, so that the bulk emulsion experiences a field-induced internal torque. The particle stress becomes a nonsymmetric stress tensor, underscoring the existence of a rotational viscosity in the bulk emulsion to satisfy the angular momentum balance. The lack of symmetry in the stress tensor of ferrofluid emulsions requires the introduction of additional material functions to fully characterize the stress state and describe the fluid rheology. For instance, Cunha *et al.* [35] used a rotational viscosity coefficient associated with the skew-symmetric part of the particle stress to assess the impact of the external field configuration on the internal torques of ferrofluid emulsions in simple shear flows.

To the best of our knowledge, the great majority of works to date focused on the dynamics of ferrofluid droplets and rheology of ferrofluid emulsions in viscometric flows such as simple shear [35–37]. However, because ferrofluid emulsions are complex fluids, the viscometric material functions obtained in simple shear cannot be extrapolated to different flows. As a macroscopic response to the imposed motion, the rheological properties reflect the dynamic behavior of the fluid microstructure. For example, the extensional rheology of complex fluids tends to be markedly different from their shear rheology counterpart because the fluid microstructure is severely more stretched in extension than in shear [53–55]. Needless to say, extensional flows of different types are paramount both in nature and industrial applications, where complex fluids such as emulsions and ferrofluids are ubiquitous [56,57].

Here we present the first three-dimensional computational study of the effects of uniform magnetic fields on the dynamics of superparamagnetic ferrofluid droplets and rheology of dilute ferrofluid emulsions in planar extensional flows. We show that the droplet shape and magnetization are tightly coupled and strongly depend on the external field intensity and direction relative to the flow. We also show that the droplet response at the microscopic level directly correlates with the rheological response of the bulk emulsion at the macroscopic level. Despite the fact that the imposed motion is purely extensional by construction, we find that the droplet tilts in the flow when the external field is not aligned with one of the flow main directions, causing notable changes in the recirculation pattern and flow topology inside the droplet. Similarly to what happens in shear flows, the system experiences a field-induced magnetic torque because of a misalignment between the droplet magnetization and the external field direction. This leads to the remarkable development of nonsymmetric shear stresses in the bulk emulsion to sustain the imposed extension. In addition to the two usual extensional viscosities associated with the normal stresses in extension, we introduce new material functions such as shear and rotational viscosities to account for the unexpected shear stresses and fully characterize the fluid stress state. We then discuss in detail the emergence of novel rheological signatures of ferrofluid emulsions subjected to external magnetic fields in planar extensional flows, highlighting their potential as a new model system for chiral fluids with internal rotational degrees of freedom.

The remainder of this article is organized as follows: the model, boundary conditions, and relevant dimensionless parameters are described in Sec. II, validation tests for the computational method are outlined in Sec. III, results are presented and discussed in Sec. IV, and some concluding remarks are given in Sec. V.

II. MATHEMATICAL MODELING

Figure 1 shows a sketch of the problem, which starts with a single ferrofluid droplet suspended in a nonmagnetizable fluid. The system is subjected to a planar extensional flow imposed in the xy plane and a uniform magnetic field \mathbf{H}_0 applied externally. The two phases are incompressible Newtonian liquids of same density ρ and viscosity η ; therefore, buoyancy effects are absent and the dispersed-to-continuous phase viscosity ratio is $\lambda = 1$. We keep the viscosity ratio constant and equal to one to isolate the effects induced by the external magnetic field, which is consistent with previous studies of ferrofluid droplets in shear flows ($\lambda = 1$ –2) [33–43]. The droplet is initially spherical, has radius a , and is located at the center of a three-dimensional box. We set the domain

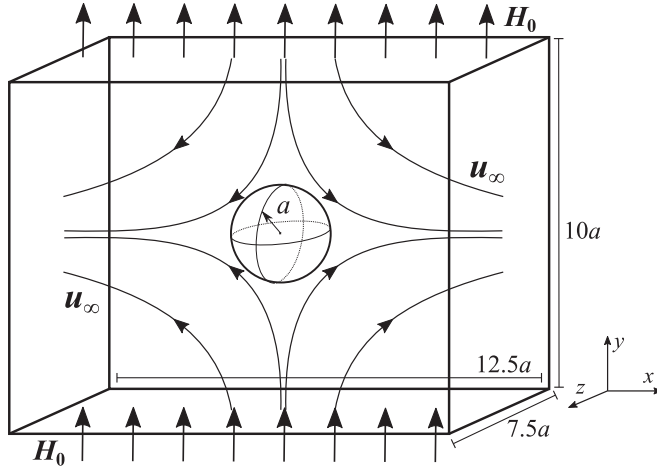


FIG. 1. Sketch of the problem (not to scale). A superparamagnetic ferrofluid droplet is suspended in a nonmagnetizable fluid. The two phases are incompressible Newtonian liquids of the same density and viscosity, and the dispersed-to-continuous phase magnetic permeability ratio is two. The droplet is initially spherical, has radius a , and the domain size (normalized by a) is 12.5, 10, and 7.5 in the x , y , and z direction, respectively (the droplet volume fraction is $\beta \approx 0.45\%$). The system is subjected to a planar extensional flow in the xy plane, and the far-field velocity \mathbf{u}_∞ of the continuous phase has a constant extension rate $\dot{\epsilon}$ that defines the directions of flow extension (x direction), flow compression (y direction), and neutral (z direction). The system is also subjected to a uniform magnetic field \mathbf{H}_0 applied externally (the external field is in the y direction in this sketch). The origin $\mathbf{x} = \mathbf{0}$ is fixed at the droplet center (the coordinate system at the bottom right is shown just for the sake of reference).

size to $12.5a$, $10a$, and $7.5a$ in the x , y , and z direction, respectively, which is comparable to that used in previous studies of viscous droplets in planar extensional flows and suffices to mitigate the effects of wall confinement on the droplet dynamics [58,59]. Macroscopically, the two-phase system is a dilute ferrofluid emulsion for which the droplet volume fraction is $\beta \approx 0.45\%$, so that hydrodynamic and magnetic interactions between droplets are both negligible. We now summarize the equations of the model (see Refs. [35,38,39,43] for details).

The two-phase flow is governed by the equations of mass conservation and momentum balance written as

$$\nabla \cdot \mathbf{u} = 0 \quad (1)$$

and

$$\rho \left(\frac{\partial \mathbf{u}}{\partial t} + \mathbf{u} \cdot \nabla \mathbf{u} \right) = -\nabla P + \eta \nabla^2 \mathbf{u} + \mathbf{F}_c + \mathbf{F}_m. \quad (2)$$

Here $\nabla = \partial/\partial \mathbf{x}$ is the nabla operator (\mathbf{x} is the position vector), \mathbf{u} is the velocity field, t is time, P is the pressure field, and \mathbf{F}_c and \mathbf{F}_m are, respectively, body forces per unit volume representing the capillary and magnetic forces in the system.

We assume that the system is at the magnetostatic limit, so that electric fields and currents are absent. At this condition, Maxwell's equations of electromagnetism reduce to $\nabla \cdot \mathbf{B} = 0$ and $\nabla \times \mathbf{H} = \mathbf{0}$, where \mathbf{B} is the magnetic induction field and \mathbf{H} is the magnetic (or magnetizing) field; note that $\mathbf{H} = -\nabla \psi$ because of the curl-free constraint, where ψ is the scalar magnetic potential. We also assume that the ferrofluid is a superparamagnetic material for which the magnetization is a linear function of the local magnetic field; that is, the external field intensity is sufficiently small to keep the ferrofluid magnetization far below the saturation magnetization, so that the classical Langevin theory of paramagnetism is approximately linear [1]. Hence, the magnetization and

magnetic fields inside the droplet are related by $\mathbf{M} = \chi\mathbf{H}$, where χ is the magnetic susceptibility. We take $\chi = 1$, so that the dispersed-to-continuous phase magnetic permeability ratio is $\zeta = 2$. We keep the permeability ratio constant and equal to two to stay reasonably consistent with previous experiments of ferrofluid droplets in quiescent liquids ($\chi = 0.9\text{--}2.2$) [18,19,21] and simulations of ferrofluid droplets in shear flows ($\chi = 0.5\text{--}1$) [33–43]. Finally, as $\mathbf{B} = \mu_0(\mathbf{M} + \mathbf{H})$, Maxwell's equations further simplify to

$$\nabla \cdot (\zeta(\mathbf{x})\nabla\psi) = 0, \quad (3)$$

where $\zeta(\mathbf{x})$ is a local version of the permeability ratio, so that $\zeta(\mathbf{x}) = 1 + \chi$ inside the droplet and $\zeta(\mathbf{x}) = 1$ in the continuous phase.

The droplet surface is captured with the level set method, which relies on a level set function $\phi(\mathbf{x}, t)$ that returns the signed distance of any point in the flow domain to the interface, so that $\phi = 0$ at the interface, $\phi < 0$ inside the droplet, and $\phi > 0$ in the continuous phase [60–62]. The outward unit normal and mean curvature of the droplet surface are $\hat{\mathbf{n}} = \nabla\phi/\|\nabla\phi\|$ and $\kappa = \nabla \cdot \hat{\mathbf{n}}$, respectively. The capillary force is $\mathbf{F}_c = -\sigma\kappa\delta(\phi)\hat{\mathbf{n}}$ and corresponds to the normal stress jump across a curved interface (the Young-Laplace equation) [60], where σ is the interfacial tension coefficient (assumed to be constant) and $\delta(\phi)$ is the Dirac delta function of ϕ . The magnetic force is $\mathbf{F}_m = \mu_0(\zeta(\mathbf{x}) - 1)\mathbf{H} \cdot \nabla\mathbf{H}$ and represents a field-induced magnetic traction that depends on the intensity and gradients of the local magnetic field (the Kelvin force) [1], where μ_0 is the magnetic permeability of the continuous phase (assumed to be equal to that of the free space). Note that a constitutive equation for the Maxwell stress tensor is not required [63]; additionally, $\zeta(\mathbf{x}) = 1 + \chi[1 - \mathcal{H}(\phi)]$, where $\mathcal{H}(\phi)$ is the Heaviside step function of ϕ . It is worth mentioning that \mathbf{F}_c and \mathbf{F}_m are both concentrated at the droplet surface. The level set function is also used to define regularized versions of the Heaviside and Dirac functions, say, $\mathcal{H}_\varepsilon(\phi)$ and $\delta_\varepsilon(\phi)$, over a thin region of thickness 2ε across the interface. Following the literature of level set methods for multiphase flows, we set

$$\mathcal{H}_\varepsilon(\phi) = \begin{cases} 0, & \text{if } \phi < -\varepsilon, \\ \frac{1}{2}\left[1 + \frac{\phi}{\varepsilon} - \frac{1}{\pi} \sin\left(\frac{\pi\phi}{\varepsilon}\right)\right], & \text{if } |\phi| \leq \varepsilon, \\ 1, & \text{if } \phi > \varepsilon, \end{cases} \quad (4)$$

where $\delta_\varepsilon(\phi) = \mathcal{H}'_\varepsilon(\phi)$ (the prime denotes derivative with respect to ϕ), and $\varepsilon = 1.5\Delta x$, where Δx is the meshing size [60]. The impulse $\delta(\phi)$ and the piecewise constant $\zeta(\mathbf{x})$ are then replaced by $\delta_\varepsilon(\phi)$ and $\zeta_\varepsilon(\phi) = 1 + \chi[1 - \mathcal{H}_\varepsilon(\phi)]$, so that \mathbf{F}_c and \mathbf{F}_m vary smoothly across the interface and vanish both inside and outside the droplet. In conclusion, the capillary and magnetic forces at the droplet surface are

$$\mathbf{F}_c = -\sigma\kappa\delta_\varepsilon(\phi)\hat{\mathbf{n}} \quad (5)$$

and

$$\mathbf{F}_m = \mu_0(\zeta_\varepsilon(\phi) - 1)\mathbf{H} \cdot \nabla\mathbf{H}. \quad (6)$$

In summary, the model consists of Eqs. (1) and (2) coupled with Eqs. (5) and (6) for the two-phase flow and Eq. (3) with $\zeta_\varepsilon(\phi)$ instead of $\zeta(\mathbf{x})$ for the magnetic potential. The system is initially at rest; the extensional flow and the external magnetic field are applied simultaneously at $t = 0$. The external field is imposed through a constant magnetic potential flux at the six boundaries (either homogeneous or nonhomogeneous von Neumann conditions, as determined by the external field direction). Velocity and pressure are periodic in the z direction; at the other four boundaries, the normal flux of the pressure gradient vanishes (homogeneous von Neumann conditions), and the velocity is imposed essentially (Dirichlet conditions). The velocity field of the continuous phase at the boundaries is a planar extension given by $\mathbf{u}_\infty = \dot{\varepsilon}(x\hat{\mathbf{e}}_x - y\hat{\mathbf{e}}_y)$, where $\hat{\mathbf{e}}_x$ and $\hat{\mathbf{e}}_y$ are the unit vectors in the x and y direction, respectively. The extension rate $\dot{\varepsilon} > 0$ is constant and defines the

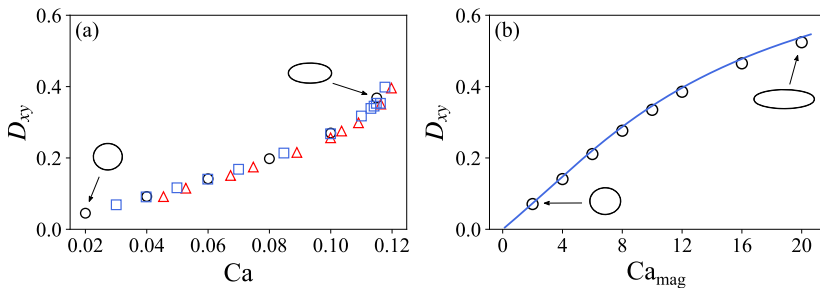


FIG. 2. (a) Droplet distortion in the xy plane (D_{xy}) as a function of Ca with no external magnetic field ($Ca_{mag} = 0$): present work (black circles), experimental results of Hsu and Leal [58] (red triangles), and simulation results of Hoang and Park [59] (blue squares). The insets show the droplet cross section in the xy plane at $Ca = 0.02$ and $Ca = 0.115$. (b) Droplet distortion in the xy plane (D_{xy}) as a function of Ca_{mag} when the external magnetic field is applied in the x direction with no external flow ($\mathbf{u}_\infty = \mathbf{0}$): present work (black circles) and theoretical predictions of Afkhami *et al.* [21] (blue line). The insets show the droplet cross section in the xy plane at $Ca_{mag} = 2$ and $Ca_{mag} = 20$.

flow three main directions, namely, flow extension (x direction), flow compression (y direction), and neutral (z direction).

The problem is governed by three dimensionless parameters: the Reynolds number, $Re = \rho a^2 \dot{\epsilon} / \eta$, which measures the ratio of inertial to viscous forces at the droplet scale; the capillary number, $Ca = \eta a \dot{\epsilon} / \sigma$, which measures the ratio of viscous to capillary forces at the droplet surface; and the magnetic capillary number, $Ca_{mag} = \mu_0 a \|\mathbf{H}_0\|^2 / \sigma$, which measures the ratio of magnetic to capillary forces at the droplet surface. We set $Re = 0.01$ to mitigate inertial effects. The other parameters, Ca and Ca_{mag} , as well as the external field direction, are changed systematically throughout this study. All variables are dimensionless henceforth.

III. CODE VALIDATION

The model is solved with the numerical scheme described by Abicalil *et al.* [38] (see Appendix A for a review). Here we focus on two validation tests: one for the flow-induced distortion of a viscous droplet in planar extension and one for the field-induced distortion of a ferrofluid droplet in a quiescent liquid. The droplet distortion is measured with a scalar parameter similar to that introduced by Taylor [31,32]. We define $D_{xy} = (L_x - L_y) / (L_x + L_y)$, where L_x and L_y are the droplet semiaxes in the x and y axis, respectively. Note that D_{xy} is a measure of planar distortion in the xy plane; we define analogous quantities to measure the droplet distortion in other planes later. We determine the steady state when the droplet shape changes in less than 0.5% between two consecutive units of dimensionless time. Figure 2 presents the results of the two tests at the steady state.

Figure 2(a) shows D_{xy} as a function of Ca with no external field ($Ca_{mag} = 0$). We also present the experimental results of Hsu and Leal [58] (measured in a four-roll mill apparatus) and the simulation results of Hoang and Park [59] (computed with a commercial software). The droplet is stretched in the x direction and, because of incompressibility, compressed in the other two directions with slightly different intensities. As a result, the droplet assumes the shape of a prolatelike ellipsoid and distorts progressively more as Ca increases. The droplet does not achieve a steady shape at $Ca \geq 0.12$; alternatively, it continuously distorts and develops necking regions near the tips in the x axis. This suggests that the droplet will eventually burst, as predicted by the earlier theoretical work of Rallison [64].

Figure 2(b) shows D_{xy} as a function of Ca_{mag} with no external flow ($\mathbf{u}_\infty = \mathbf{0}$). The external field direction is not important here; we conveniently apply the external field in the x direction to keep D_{xy}

as the main measure of droplet distortion. We also present the theoretical predictions of Afkhami *et al.* [21] for the droplet shape at equilibrium. The agreement between the results is again excellent (within $\sim 1.5\%$). As we detail later, the external field induces a magnetic force normal to the droplet surface because the difference in magnetic permeability between the phases leads to a magnetic field jump across the interface; this force is stronger in regions where the interface is perpendicular to the external field direction. In the absence of external flow, the field-induced distortion corresponds to a uniaxial extensional loading; that is, the droplet is stretched in the x direction and, because of incompressibility, compressed in the other two directions with equal intensities. As a result, the droplet assumes the shape of a prolate ellipsoid and distorts progressively more as Ca_{mag} increases. We observe no signs of hysteresis nor the formation of conical tips in the droplet shape up to $\text{Ca}_{\text{mag}} = 20$, which agrees with previous studies of low to moderate field-induced distortion ($D_{xy} \lesssim 0.6$) of superparamagnetic droplets with small to medium magnetic susceptibilities ($\chi \lesssim 20$) [27].

The results of Figs. 2(a) and 2(b) have an important qualitative difference. In both cases, there is an initial range where D_{xy} increases close to linearly with the corresponding parameter under study, either Ca or Ca_{mag} . However, Fig. 2(a) shows that D_{xy} displays a nonlinear, softeninglike response when Ca is sufficiently high. There is a critical value of Ca above which a further increase in Ca enhances the flow-induced distortion. This is likely related to the existence of an upper limit of Ca around $\text{Ca} \approx 0.12$ above which the droplet does not achieve a steady shape and eventually bursts. In contrast, Fig. 2(b) shows that D_{xy} displays a nonlinear, hardeninglike response when Ca_{mag} is sufficiently high. This leads to an asymptotic value for D_{xy} at the limit of very high Ca_{mag} . The theory of Afkhami *et al.* [21] indicates that $D_{xy} \rightarrow 1$ as $\text{Ca}_{\text{mag}} \rightarrow \infty$, a condition at which the droplet approaches a very slender prolate ellipsoid aligned with the external field direction. We revisit these points later. For now, the agreement with previous studies in the literature confirms the reliability of our simulation results regarding the hydrodynamic, magnetic, and interfacial problems.

IV. RESULTS AND DISCUSSIONS

We split this section in two parts. First, we discuss the results for which the external magnetic field is applied in one of the flow three main directions (extension, compression, or neutral, as defined by the x , y , and z axis, respectively). Second, we discuss the results for which the external field is in a direction different from one of the flow main directions. We focus on the effects of the external field configuration (intensity and direction) on the droplet shape and magnetization, as well as on the planar extensional rheology of the resulting ferrofluid emulsion. Our analyses are for $\text{Ca} \leq 0.12$ and $\text{Ca}_{\text{mag}} \leq 20$, and all results correspond to the steady state.

A. External magnetic fields applied in one of the flow main directions

1. Droplet shape and magnetization

Figure 3 shows the droplet distortion in the xy plane, D_{xy} , as a function of Ca_{mag} . The results are for different values of Ca when the external magnetic field is applied in the x and y direction. We see that D_{xy} grows with Ca_{mag} when the external field is in the x direction [Fig. 3(a)]. Because viscous and magnetic forces stretch the droplet together in the same direction, the droplet assumes a prolatelike shape with the major axis in the x axis ($D_{xy} > 0$). This field-induced extension is slightly more pronounced in strong flows (high Ca). In turn, D_{xy} falls with Ca_{mag} when the external field is in the y direction [Fig. 3(b)]. Viscous and magnetic forces now compete to stretch the droplet in directions that are perpendicular to one another. Briefly, the field-induced extension in the y direction is counteracted by flow-induced compression, whereas the flow-induced extension in the x direction is counteracted by field-induced compression. At low enough Ca_{mag} , viscous forces dominate over magnetic forces, and the droplet major axis is in the x axis ($D_{xy} > 0$). As Ca_{mag} increases and the external field intensity grows stronger, magnetic forces eventually overtake viscous forces and the

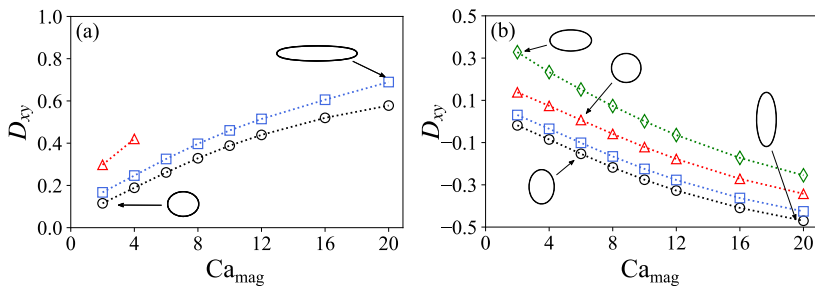


FIG. 3. Droplet distortion in the xy plane (D_{xy}) as a function of Ca_{mag} when the external magnetic field is applied in the (a) x direction and (b) y direction. The results are for $Ca = 0.02$ (black circles), $Ca = 0.04$ (blue squares), $Ca = 0.08$ (red triangles), and $Ca = 0.12$ (green diamonds). The insets show the droplet cross section in the xy plane at different conditions. The data set is not complete in (a) because the droplet does not achieve a steady shape when $Ca = 0.08$ and $Ca_{\text{mag}} \geq 6$ and when $Ca = 0.12$ and $Ca_{\text{mag}} \geq 0$ [see the discussion for Fig. 2(a)].

droplet major axis becomes aligned with the y axis ($D_{xy} < 0$). This field-induced shape transition is easier in weak flows (low Ca).

Figure 4 shows the droplet distortion as a function Ca_{mag} for different values of Ca when the external magnetic field is applied in the z direction. Note that we now plot D_{xy} and $D_{xz} = (L_x - L_z)/(L_x + L_z)$, where L_z is the droplet semiaxis in the z axis. We observe that D_{xy} is a weak function of Ca_{mag} [Fig. 4(a)]. The field-induced compression in the x and y direction is approximately the same, particularly at low Ca [see the discussion for Fig. 2(b)]. Thus, the droplet distortion in the xy plane is mainly governed by the balance between viscous and capillary forces, as determined by Ca . Conversely, D_{xz} falls strongly with Ca_{mag} [Fig. 4(b)]. The competition between viscous and magnetic forces behind this field-induced shape transition—from $D_{xz} > 0$ with the droplet major axis in the x axis to $D_{xz} < 0$ with the droplet major axis in the z axis—is similar to that discussed for Fig. 3(b). The major difference here is that D_{xz} is a weaker function of Ca , especially at high Ca_{mag} , where all curves approach one another. This indicates that viscous forces play a minor role in the droplet distortion in the direction of the external magnetic field when the latter is sufficiently strong and aligned with the flow neutral direction.

Figures 3 and 4 suggest that the intensity and direction of external magnetic fields can be adjusted to either induce or prevent droplet breakup in planar extensional flows. Recall that the droplet bursts at $Ca \approx 0.12$ in the absence of an external field ($Ca_{\text{mag}} = 0$) [see the discussion for Fig. 2(a)]. On the

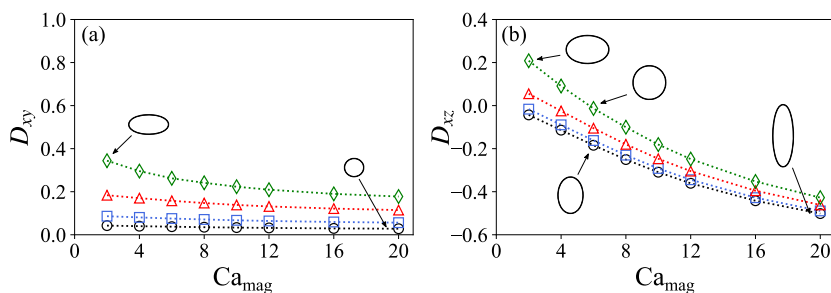


FIG. 4. Droplet distortion in the (a) xy plane (D_{xy}) and (b) xz plane (D_{xz}) as a function of Ca_{mag} when the external magnetic field is applied in the z direction. The results are for $Ca = 0.02$ (black circles), $Ca = 0.04$ (blue squares), $Ca = 0.08$ (red triangles), and $Ca = 0.12$ (green diamonds). The insets show the droplet cross section in the (a) xy plane and (b) xz plane at different conditions.

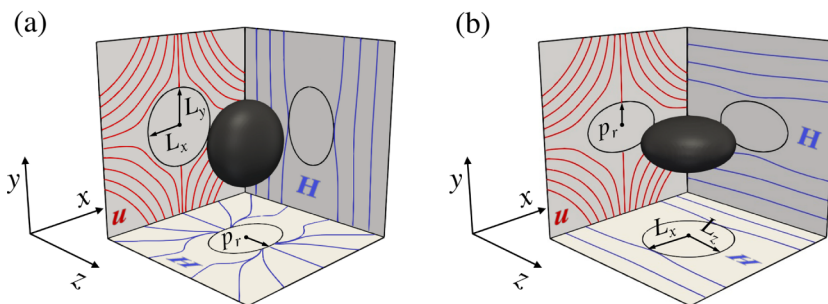


FIG. 5. Three-dimensional view of oblate droplets at $Ca = 0.12$ when the external magnetic field is applied in the (a) y direction (at $Ca_{\text{mag}} = Ca_{\text{mag}}^* \approx 10.03$) and (b) z direction (at $Ca_{\text{mag}} = Ca_{\text{mag}}^* \approx 5.74$). In (a) $L_x = L_y$ is the equatorial radius in the xy plane and p_r is the polar radius in the z axis; in (b) $L_x = L_z$ is the equatorial radius in the xz plane and p_r is the polar radius in the y axis. For the sake of visualization, the droplet shape is projected on each plane (black), flow streamlines outside the droplet are projected on the xy plane (red), and magnetic field lines outside the droplet are projected on the yz and xz plane (blue).

one hand, we find that the droplet does not achieve a steady shape at $Ca = 0.08$ when the external field is in the x direction at $Ca_{\text{mag}} \geq 6$, indicating that the droplet will eventually breakup. On the other hand, we do observe steady shapes with no signs of droplet breakup at $Ca = 0.12$ when the external field is either in the y or z direction at $Ca_{\text{mag}} \geq 2$. It is worth noticing that the breakup is not strictly associated with the droplet distortion. Whereas Fig. 2(a) shows that $D_{xy} \approx 0.4$ immediately before the breakup at $Ca \approx 0.12$ and $Ca_{\text{mag}} = 0$, Figs. 3 and 4 confirm that the droplet can sustain larger distortions with a steady shape depending on the external field configuration; for instance, $D_{xy} \approx 0.7$ at $Ca = 0.04$ when the external field is in the x direction at $Ca_{\text{mag}} = 20$ [see Fig. 3(a)]. The potential of controlling the breakup dynamics of ferrofluid droplets with external magnetic fields was originally addressed by Cunha *et al.* [39] for simple shear flows. Yet a detailed analysis of this field-mediated breakup control requires an extensive study over a multidimensional parameter space that involves not only Re , Ca , Ca_{mag} , and the external field direction, but also λ and ζ . This is beyond the scope of this work.

The field-induced shape transition presented in Figs. 3(b) and 4(b) also deserves special remarks. We build the discussion based on the results of Fig. 3(b), for which the external field is in the y direction. At fixed Ca , there is a specific value of Ca_{mag} , say Ca_{mag}^* , at which the droplet cross section in the xy plane is circular because the semiaxes in the x and y axis are equal ($D_{xy} = 0$ when $L_x = L_y$). At this condition, the net effects of field-induced extension in the y direction and flow-induced extension in the x direction match one another. Because both viscous and magnetic forces compress the droplet together in the z direction, the droplet becomes an oblate ellipsoid with a polar radius $p_r = L_z$ in the z axis. A similar rationale applies when the external field is in the z direction, as in Fig. 4(b). The only difference is that the circular cross section is in the xz plane ($D_{xz} = 0$ when $L_x = L_z$) and the polar radius is $p_r = L_y$ in the y axis. To ease the visualization, Fig. 5 displays a three-dimensional view of oblate droplets at $Ca = 0.12$ (and $Ca_{\text{mag}} = Ca_{\text{mag}}^*$) for the two external field configurations. Additionally, Fig. 6 shows how Ca_{mag}^* and p_r depend on Ca . Interestingly, both Ca_{mag}^* and p_r vary linearly with Ca , at least within the range of parameters explored here (see the caption of Fig. 6 for details). We note that Ca_{mag}^* increases and p_r decreases with Ca . Because viscous and magnetic forces stretch the droplet in directions that are perpendicular to one another, the magnetic force required to promote a circular droplet cross section in a plane—either xy or xz —increases as the relative intensity of viscous forces grows stronger. The equatorial radius—either $L_x = L_y$ in the xy plane or $L_x = L_z$ in the xz plane—also increases with the intensity of viscous forces, so that the polar radius—either $p_r = L_z$ in the z axis or $p_r = L_y$ in the y axis—decreases to preserve the droplet volume. At fixed Ca , we see that Ca_{mag}^* and p_r are higher for external fields in the y direction. This is not unexpected, as the field-induced

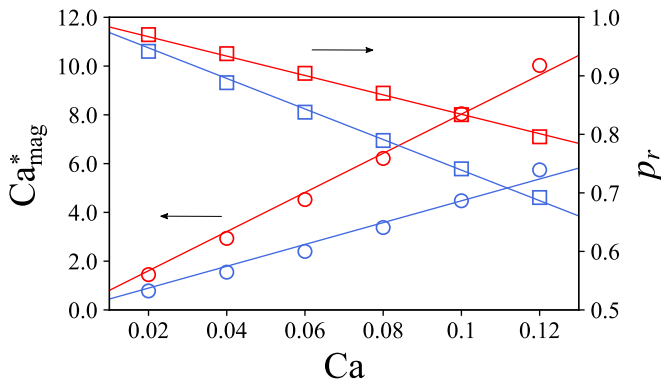


FIG. 6. Magnetic capillary number Ca_{mag}^* at which the droplet becomes an oblate ellipsoid (circles, left axis) and the corresponding droplet polar radius p_r (squares, right axis) as a function of Ca . The results are for external magnetic fields applied in the y direction (red symbols) and z direction (blue symbols). The solid lines are linear fits with fixed intercepts ($Ca_{\text{mag}}^* = 0$ and $p_r = 1$ at $Ca = 0$): $Ca_{\text{mag}}^* \approx 80Ca$ and $p_r \approx 1 - 1.7Ca$ when the external field is in the y direction (red); $Ca_{\text{mag}}^* \approx 44Ca$ and $p_r \approx 1 - 2.6Ca$ when the external field is in the z direction (blue). The coefficient of determination of all adjustments is $R^2 > 0.99$.

extension is more attenuated by the flow-induced compression in this case. The reader interested in the shape control of liquid droplets through external force fields in hydrodynamic flows is referred to Liu *et al.* [65], who recently presented a study of the electric field-mediated spheroidization of leaky dielectric droplets in uniaxial extensional flows.

Overall, the droplet shape is determined by a balance between viscous, magnetic, and capillary forces that depends on the external field intensity and direction relative to the flow. As earlier noted by Jesus *et al.* [30], and further confirmed here, three-dimensional computational studies are critical to accurately predict and fundamentally understand the dynamics of ferrofluid droplets in external magnetic fields and hydrodynamic flows. Three-dimensional simulations unveil a complex physics of which most details would be either poorly addressed or even missed in their two-dimensional counterparts. The present discussions can bring new insights to improve the field-assisted manufacturing of microparticles for which shape–property relationships can be broadly explored based on the magnetic–hydrodynamic coupling of ferrofluids and nonmagnetizable liquids [66,67].

Before moving forward, we must also highlight that in all cases analyzed thus far the droplet remains symmetric with respect to the three main directions set by the planar extensional flow. That is, the droplet distorts and assumes the shape of an ellipsoid that, albeit not generally axisymmetric, retains its main axes aligned with the x , y , and z axis. Figure 7 shows the z component of the flow vorticity $\xi = \nabla \times \mathbf{u}$ and flow streamlines near the droplet in the xy plane. The results are for $Ca = 0.04$ when the external field is absent ($Ca_{\text{mag}} = 0$) [Fig. 7(a)] and when the external field is applied in one of the flow main directions at $Ca_{\text{mag}} = 16$ [Figs. 7(b)–7(d)]. The magnetic field does not change the general flow pattern. Even though the way the distorted droplet affects the streamlines near the interface depends on the external field direction, the flow inside the droplet remains characterized by four recirculation regions that are symmetric with respect to the reference axes, as in the absence of the external field. This is the same flow pattern reported by Liu *et al.* [65] for leaky dielectric droplets in uniaxial extensional flows both in the absence and in the presence of external electric fields applied in the extension and compression directions.

We now examine the magnetization of ferrofluid droplets and emulsions. The mean magnetization of the system is [35,38]

$$\langle \mathbf{M} \rangle = \frac{1}{V} \int_V (\xi(\mathbf{x}) - 1) \mathbf{H} dV, \quad (7)$$

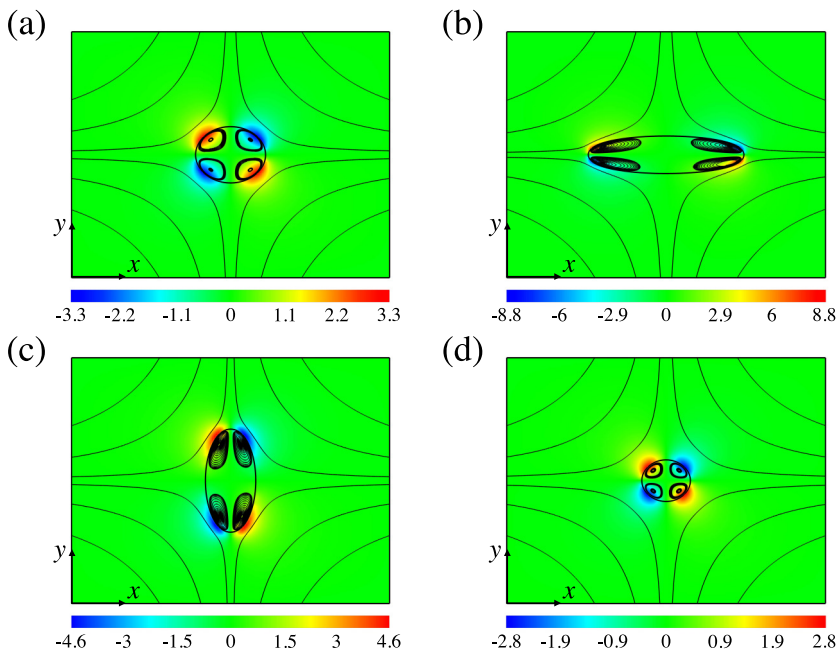


FIG. 7. z component of the flow vorticity ($\xi = \nabla \times \mathbf{u}$) and flow streamlines in the xy plane. The results are for $Ca = 0.04$ when (a) there is no external magnetic field ($Ca_{\text{mag}} = 0$) and when the external magnetic field is applied in the (b) x direction, (c) y direction, and (d) z direction at $Ca_{\text{mag}} = 16$.

where V is the total volume occupied by the two phases. Note that the continuous phase does not contribute to the system magnetization and that $\zeta(\mathbf{x})$ is replaced by $\zeta_\varepsilon(\phi)$ for calculations. Macroscopically, the ferrofluid emulsion magnetizes only because the dispersed phase consists of ferrofluid droplets and the system is subjected to an external magnetic field. Equation (7) is, in essence, a volumetric average of the magnetization of a single droplet in suspension. The bulk magnetization of the ferrofluid emulsion is $\langle \mathbf{M} \rangle = \beta \mathbf{M}$, where β is the droplet volume fraction and $\mathbf{M} = \chi \mathbf{H}$ is the droplet magnetization.

Ellipsoids are the only finite bodies that can be uniformly magnetized in uniform magnetic fields [68,69]. Therefore, the magnetic field inside a prolate ferrofluid droplet in a quiescent liquid subjected to a relatively weak uniform magnetic field is uniform and parallel to the external field direction [27]. The same holds true for ferrofluid droplets in planar extensional flows when the external field is applied in one of the flow main directions. Figure 8 shows the magnetic field intensity and lines near the droplet in the xy plane for $Ca_{\text{mag}} = 12$ with no external flow ($\mathbf{u}_\infty = \mathbf{0}$) [Fig. 8(a)] and with the external flow at $Ca = 0.04$ [Figs. 8(b)–8(d)]. The flow does not change the general behavior of the magnetic field in the system. Far outside the droplet, the magnetic field is uniform and equal to the external field because the continuous phase is a nonmagnetizable fluid. Inside the droplet, the magnetic field is uniform and parallel to the external field direction because the droplet behaves like a magnetizable ellipsoid; as we discuss shortly, the lower field intensity inside the droplet results from a demagnetizing factor that depends on the droplet shape and orientation. Outside the droplet and close to the interface, the magnetic field is not uniform. The field lines are deflected near the droplet because of the difference in magnetic permeability between the phases; the spatial gradients associated with the magnetic field discontinuity across the interface are the source of the field-induced magnetic force at the droplet surface [see Eq. (6)]. The field intensity outside the droplet is higher/lower in regions where the interface is normal/tangent

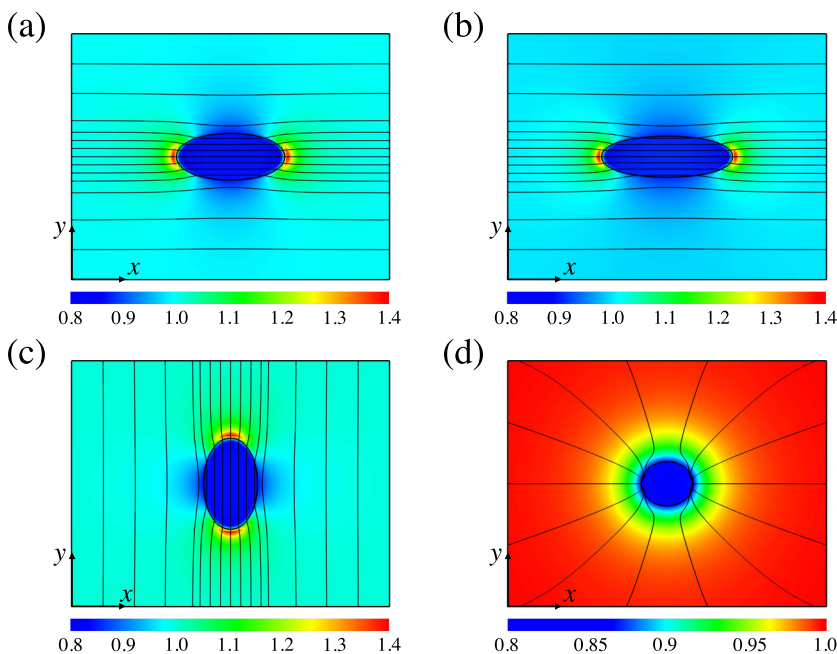


FIG. 8. Magnitude of the magnetic field and magnetic field lines in the xy plane. The results are for $Ca_{\text{mag}} = 12$ when (a) the external magnetic field is applied in the x direction with no external flow ($\mathbf{u}_{\infty} = \mathbf{0}$) and when the external magnetic field is applied in the (b) x direction, (c) y direction, and (d) z direction with the external flow at $Ca = 0.04$.

to the external field. These are the regions where the magnetic force is stronger/weaker; because of symmetry, these are also the regions where the droplet curvature is maximum/minimum.

The demagnetizing factor of a general ellipsoid decreases as the ellipsoid slims and approaches a slender body aligned with the external field [68,69]. Similarly, the demagnetizing factor of a prolate ferrofluid droplet in a quiescent liquid decreases with the droplet eccentricity, so that the droplet magnetization increases as the external field intensity grows and the droplet becomes more elongated in the external field direction [27]. Figure 9 shows the magnitude of the droplet magnetization, $M = \|\mathbf{M}\|$, as a function of Ca_{mag} for different values of Ca . We note that M grows monotonically with Ca_{mag} independently of the external field direction. Increasing the external field intensity increases the droplet elongation in the external field direction [see Figs. 3 and 4(b)]; this

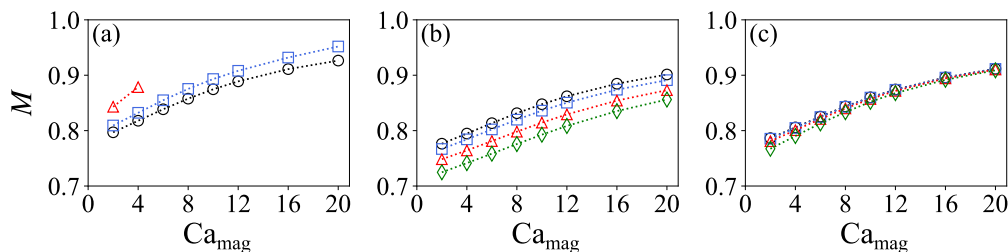


FIG. 9. Magnitude of the droplet magnetization (M) as a function of Ca_{mag} when the external magnetic field is applied in the (a) x direction, (b) y direction, and (c) z direction. The results are for $Ca = 0.02$ (black circles), $Ca = 0.04$ (blue squares), $Ca = 0.08$ (red triangles), and $Ca = 0.12$ (green diamonds).

decreases the demagnetizing factor and increases the droplet magnetization. Viscous forces play a role in the droplet shape and affect the demagnetizing factor as well. Yet the way M trends with Ca essentially depends on the external field direction. We see that M increases with Ca when the external field is in the x direction [Fig. 9(a)]. The flow improves the droplet magnetization because viscous and magnetic forces stretch the droplet together in the same direction, increasing the overall droplet elongation in the external field direction [see Fig. 3(a)]. Conversely, M decreases with Ca when the external field is in the y direction [Fig. 9(b)]. The flow hinders the droplet magnetization because viscous and magnetic forces compete to stretch the droplet in different directions that are perpendicular to one another, decreasing the overall droplet elongation in the external field direction [see Fig. 3(b)]. All M vs Ca_{mag} curves collapse when the external field is in the z direction [Fig. 9(c)]. The flow is not consequential to the droplet magnetization because viscous forces have a minor effect on the droplet elongation in the external field direction when the latter is in the neutral direction [see Fig. 4(b)]. In all cases, the rate at which M grows with Ca_{mag} decreases as Ca_{mag} increases; at finite Ca , we expect $M \rightarrow 1$ as $\text{Ca}_{\text{mag}} \rightarrow \infty$, which corresponds to the magnetization counterpart of the hardeninglike behavior observed in Fig. 2(b).

Because $\langle \mathbf{M} \rangle = \beta \mathbf{M}$ for the bulk system, ferrofluid emulsions of superparamagnetic droplets behave as a superparamagnetic material for which the effective magnetic susceptibility increases with β and M . Because M is determined by the coupling between viscous, magnetic, and capillary forces at the droplet level, the magnetic susceptibility of the bulk emulsion varies with the external field configuration, even if the magnetic susceptibility of the constituent droplets is constant. These predictions agree qualitatively well with previous theoretical and experimental studies of static magnetic properties of ferrofluid emulsions in relatively weak magnetic fields, below the saturation magnetization of the ferrofluid droplets in suspension [70–73].

2. Emulsion rheology

We now study the impact of external magnetic fields on the planar extensional rheology of dilute ferrofluid emulsions. The dimensionless particle stress associated with ferrofluid droplets in suspension is [35] (see Appendix B for details)

$$\boldsymbol{\sigma}^d = \frac{1}{V} \int_S \left[\left(\frac{\kappa}{\text{Ca}} - \frac{\text{Ca}_{\text{mag}}}{2\text{Ca}} (\zeta - 1) \|\mathbf{H}\|^2 \right) \mathbf{x}\hat{\mathbf{n}} \right] dS, \quad (8)$$

where S is the droplet surface. Note that a , $\eta\dot{\epsilon}$, and H_0 are used as characteristic scales of length, stress, and magnetic field intensity to normalize $\boldsymbol{\sigma}^d$, respectively, and that ζ is replaced by $\zeta_\epsilon(\phi)$ for calculations. For the sake of convenience, we will refer to $\boldsymbol{\sigma}^d$ as the droplet stress, as it measures the contribution of the ferrofluid droplets to the bulk stress tensor of the resulting ferrofluid emulsion when the two-phase system is taken as a homogeneous material from a continuum perspective. Equation (8) is valid only for $\lambda = 1$; the interested reader is referred to the original work of Batchelor [44] for details on the particle stress of general particulate systems. The droplets affect the stress tensor of the bulk emulsion only through capillary and magnetic forces acting at the fluid interface; the dyadic $\mathbf{x}\hat{\mathbf{n}}$ captures anisotropic contributions to the stress associated with the droplet shape. Because the droplet is symmetric with respect to the reference axes, the normal components of $\mathbf{x}\hat{\mathbf{n}}$ are all positive. The shear components of $\mathbf{x}\hat{\mathbf{n}}$ change in sign along the interface, but these changes are antisymmetric. As both κ and $\|\mathbf{H}\|^2$ are positive and symmetric with respect to the reference axes (see Fig. 8), the shear components of the integrals of $\kappa\mathbf{x}\hat{\mathbf{n}}$ and $\|\mathbf{H}\|^2\mathbf{x}\hat{\mathbf{n}}$ over S are null. As a result, the shear stresses of $\boldsymbol{\sigma}^d$ vanish identically, so that $\boldsymbol{\sigma}^d$ is a symmetric tensor for which the only nonzero entries are the normal stresses σ_{xx}^d , σ_{yy}^d , and σ_{zz}^d .

It is instructive to split the droplet stress into a traction term given by

$$\boldsymbol{\sigma}_t^d = \frac{1}{V} \int_S \frac{\kappa}{\text{Ca}} \mathbf{x}\hat{\mathbf{n}} dS \quad (9)$$

and a compression term by

$$\sigma_c^d = -\frac{1}{V} \int_S \frac{\text{Ca}_{\text{mag}}}{2\text{Ca}} (\zeta - 1) \|\mathbf{H}\|^2 \mathbf{x}\hat{\mathbf{n}} dS. \quad (10)$$

While the traction term depends on $1/\text{Ca}$ and contributes with positive values to the normal stresses, the compression term depends on $\text{Ca}_{\text{mag}}/\text{Ca}$ and contributes with negative values to the normal stresses. Note that $\text{Ca}_{\text{mag}}/\text{Ca}$ measures the ratio of magnetic to viscous forces at the droplet scale and does not depend on the interfacial tension between the phases. Importantly, the compression term is a direct consequence of the field-induced magnetic force at the droplet surface. Equations (9) and (10) then provide interesting insights. At fixed Ca , increasing Ca_{mag} enhances the overall compression of the stress state. In contrast, at fixed Ca_{mag} , increasing Ca mitigates both the traction and compression contributions to the stress state. If Ca_{mag} is sufficiently small, the normal stresses are positive (traction-dominated) and increasing Ca leads to lower normal stresses (less traction, more compression). If Ca_{mag} is sufficiently high, the normal stresses are negative (compression-dominated) and increasing Ca leads to higher normal stresses (less compression, more traction). We find that this transition occurs around $\text{Ca}_{\text{mag}} \approx 6$ for the cases analyzed here. The droplet shape also plays a role. First, distorted droplets are an important source of anisotropic stresses; these are captured by $\mathbf{x}\hat{\mathbf{n}}$ and affect both the traction and compression terms. When the droplet is stretched/compressed in a certain direction, the unit normal associated with this direction becomes more/less distant from the droplet center, increasing/decreasing the anisotropic contribution to the normal stress in this direction. Second, distorted droplets have a nonuniform curvature distribution over the surface, which affects the traction terms.

Usually, the steady-state rheology in planar extension is fully characterized by two extensional viscosity coefficients [56]: the planar extensional viscosity and the second extensional viscosity. Both material functions are based on the normal stresses and uniquely determine the deviatoric part of the stress tensor. The planar extensional viscosity measures the material resistance to be continuously stretched in the x direction and compressed in the y direction at the same rate, while the second extensional viscosity measures the material resistance to prevent continuous deformation in the z direction (at the same condition). In the present work, we are primarily interested in the droplet stress contributions. In this way, we define the dimensionless planar extensional viscosity,¹ $\eta_p = \sigma_{xx}^d - \sigma_{yy}^d$, and the dimensionless second extensional viscosity, $\eta_2 = \sigma_{zz}^d - \sigma_{yy}^d$, in order to measure the droplet contribution to the extensional viscosity coefficients of the bulk emulsion.

Figure 10 shows η_p (normalized by β) as a function of Ca_{mag} for different values of Ca . We start with the external field in the x direction [Fig. 10(a)]. Increasing Ca_{mag} increases the distortion of the prolatelike droplet in the x direction [see Fig. 3(a)]. The higher curvature at the droplet tips in the x axis increases the traction contribution to σ_{xx}^d . Analogously, the lower curvature at the droplet tips in the y direction decreases the traction contribution to σ_{yy}^d . The compression contribution to σ_{xx}^d is much more attenuated by the traction counterpart in comparison to what happens with σ_{yy}^d . As a result, η_p grows with Ca_{mag} , which corresponds to a field-induced viscous-hardening behavior (or a magnetic-thickening effect) [Fig. 10(a)]. Because viscous forces also stretch the droplet in the x direction [see Fig. 3(a)], the net effect of increasing Ca is an increase in the anisotropic contribution of $\mathbf{x}\hat{\mathbf{n}}$ to the traction term. Hence, η_p also grows with Ca [Fig. 10(a)]. The results with the external field in the y direction are more delicate [Fig. 10(b)]. Increasing Ca_{mag} now drives the droplet through a dramatic geometric change in the xy plane [see Fig. 3(b)]; the droplet starts as a prolatelike ellipsoid with the major axis in the x axis at low Ca_{mag} , becomes an oblate ellipsoid with the polar radius in the z axis at $\text{Ca}_{\text{mag}} = \text{Ca}_{\text{mag}}^*$, and eventually becomes a prolatelike ellipsoid with

¹The dimensional version of the droplet contribution to the planar extensional viscosity is $\eta_{p,\text{dim}} = (\sigma_{xx,\text{dim}}^d - \sigma_{yy,\text{dim}}^d)/\dot{\epsilon}$, in such manner that $\eta_p = \eta_{p,\text{dim}}/\eta$. The same applies to the droplet second extensional viscosity as well as to the shear and rotational viscosity coefficients, defined in Sec. IV B 2.

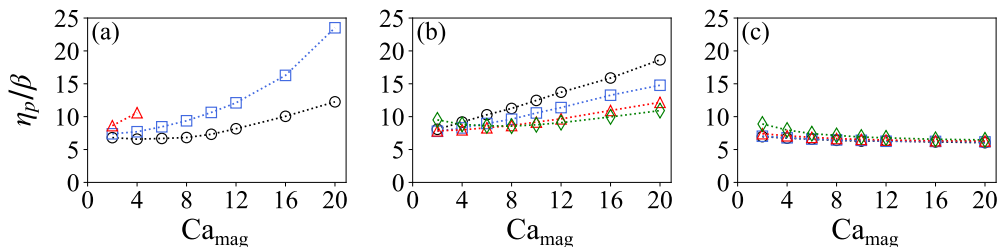


FIG. 10. Droplet contribution to the planar extensional viscosity (η_p) of the ferrofluid emulsion as a function of Ca_{mag} when the external magnetic field is applied in the (a) x direction, (b) y direction, and (c) z direction. The results are for $Ca = 0.02$ (black circles), $Ca = 0.04$ (blue squares), $Ca = 0.08$ (red triangles), and $Ca = 0.12$ (green diamonds). Note that η_p is normalized by the droplet volume fraction (β).

the major axis in the y axis at high Ca_{mag} . The anisotropic contribution of $\mathbf{x}\hat{\mathbf{n}}$ to the compression and traction terms associated with σ_{yy}^d becomes progressively more pronounced throughout this process. However, anisotropic changes in the droplet shape driven by the external field intensity are not followed by changes in curvature of similar strength because the competition between viscous and magnetic forces stretching the droplet in different directions results in less pronounced curvatures at the droplet tips. As a result, the compression contribution overcomes the traction contribution in σ_{yy}^d , so that η_p generally grows with Ca_{mag} and falls with Ca [Fig. 10(b)]; the only exception occurs at $Ca = 0.12$ for $Ca_{\text{mag}} \lesssim 6$. This viscous-hardening behavior is less apparent in strong flows because increasing Ca attenuates the imbalance of the stress state by reducing both the traction and compression terms. The results for the external field in the z direction are simpler [Fig. 10(c)]. Because both Ca_{mag} and Ca are not very consequential to the droplet shape in the xy plane [see Fig. 4(a)], η_p remains nearly constant [Fig. 10(c)].

Figure 11 shows the results for η_2 (also normalized by β) in the same fashion. To assist the discussion, Fig. 12 presents the droplet distortion in the yz plane measured with $D_{zy} = (L_z - L_y)/(L_z + L_y)$. Again, we start with the external field in the x direction [Fig. 11(a)]. Viscous and magnetic forces compress the droplet together with similar intensities in the y and z direction, so that Ca_{mag} and Ca do not induce substantial changes in the droplet shape in the yz plane [Fig. 12(a)]. It follows that η_2 is effectively constant [Fig. 11(a)]. This parallels the results for η_p when the external field is in the z direction [see Fig. 10(c)]. The reasoning behind the viscous-hardening behavior of η_2 when the external field is in the y direction [Fig. 11(b)] is similar to that discussed for η_p [see Fig. 10(b)]. That is, increasing Ca_{mag} and stretching droplet in the y direction increases the anisotropic contribution of $\mathbf{x}\hat{\mathbf{n}}$ to the compression term associated with σ_{yy}^d , which

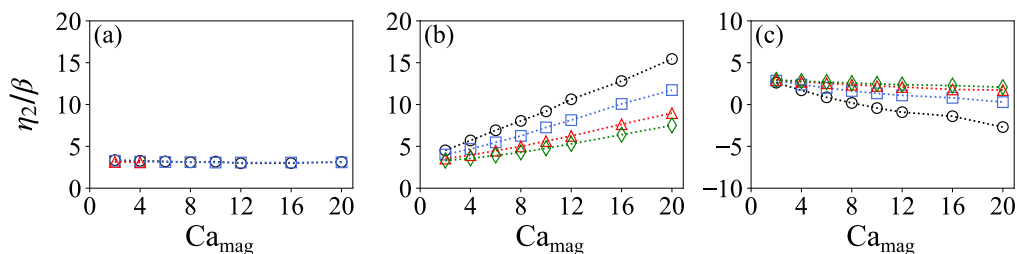


FIG. 11. Droplet contribution to the second extensional viscosity (η_2) of the ferrofluid emulsion as a function of Ca_{mag} when the external magnetic field is applied in the (a) x direction, (b) y direction, and (c) z direction. The results are for $Ca = 0.02$ (black circles), $Ca = 0.04$ (blue squares), $Ca = 0.08$ (red triangles), and $Ca = 0.12$ (green diamonds). Note that η_2 is normalized by the droplet volume fraction (β).

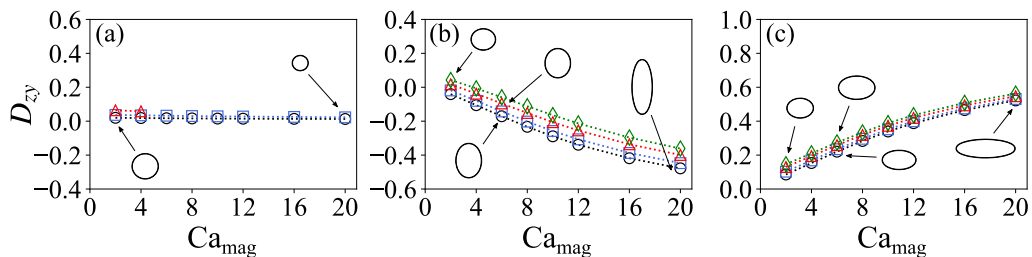


FIG. 12. Droplet distortion in the yz plane (D_{yz}) as a function of Ca_{mag} when the external magnetic field is applied in the (a) x direction, (b) y direction, and (c) z direction. The results are for $Ca = 0.02$ (black circles), $Ca = 0.04$ (blue squares), $Ca = 0.08$ (red triangles), and $Ca = 0.12$ (green diamonds). The insets show the droplet cross section in the yz plane at different conditions.

overtakes the corresponding traction term because changes in curvature are not equivalently strong [see Fig. 12(b)]. Thus, η_2 grows with Ca_{mag} and falls with Ca [Fig. 11(b)]. The same rationale applies to the field-induced viscous-softening behavior (or magnetic-thinning effect) of η_2 when the external field is in the z direction [Fig. 11(c)]. Increasing Ca_{mag} and stretching the droplet in the z direction leads to compression terms stronger than the corresponding traction terms because of insufficiently strong changes in the droplet curvature [see Fig. 12(c)]. As a result, η_2 falls with both Ca_{mag} and Ca [Fig. 11(c)].

In general, traction and compression (forces) are necessary to promote extension and compression (kinematics), respectively. Conceived as material properties, the extensional viscosities measure resistance coefficients associated with the difficulty of imposing the corresponding kinematics. Common materials, so to speak, thus possess positive extensional viscosities. In most of the cases analyzed here, the droplet contribution to the extensional viscosities of the bulk emulsion is positive and either remains constant or increases (viscous-hardening) with the external field intensity [see Figs. 10(a)–11(b)]. The fact that η_2 decreases (viscous-softening) with the external field intensity and eventually achieves negative values at low Ca and high Ca_{mag} when the external field is in the z direction [see Fig. 11(c)] deserves a special remark. In this case, increasing the external field intensity mitigates the difficulty added by the droplet in imposing the bulk extensional kinematics in the yz plane; when η_2 is negative, the droplet facilitates the bulk motion in this plane. Interestingly, this behavior is somewhat similar to what happens with some active fluids, such as suspensions of pusher microorganisms like *E. coli* and *B. subtilis* bacteria [74].

The behavior of complex fluids is a strong function of the flow kinematics. Because the rheological material functions are defined for certain flow conditions, comparing viscometric and extensional material functions is not straightforward, yet not illegitimate. Overall, the response of ferrofluid emulsions in planar extension is very different from that in simple shear, particularly regarding the dependence of the relevant material functions on Ca_{mag} and Ca for a specific external field direction. For example, as Ca_{mag} increases with the external field in the flow direction, the shear viscosity decreases and becomes less dependent of Ca , indicating a magnetic-thinning effect that eventually suppresses the usual shear-thinning behavior of dilute emulsions. Additionally, whereas the first normal stress difference in shear increases with Ca , decreases with Ca_{mag} , and achieves negative values at low Ca and high Ca_{mag} , the second normal stress difference decreases with Ca , increases with Ca_{mag} , and tends to positive values for all Ca at high Ca_{mag} . Here, in contrast, as Ca_{mag} increases with the external field in the flow extension direction, the planar extensional viscosity increases and becomes more dependent of Ca , revealing a magnetic-thickening effect that amplifies the usual extensional-thickening behavior of dilute emulsions, and the second planar extensional viscosity remains constant and approximately independent of Ca . The reader is referred to Cunha *et al.* [35] and Ishida and Matsunaga [36] for details on the shear rheology of ferrofluid emulsions subjected to uniform magnetic fields.

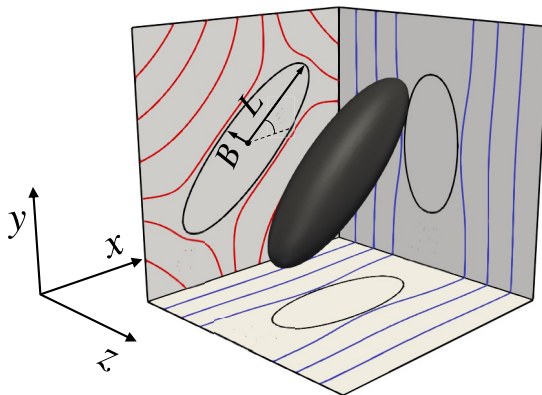


FIG. 13. Three-dimensional view of the prolatelike droplet at $Ca = 0.02$ when the external magnetic field is applied in the $x = y$ direction at $Ca_{\text{mag}} = 20$. For the sake of visualization, the droplet shape is projected on each plane (black), flow streamlines outside the droplet are projected on the xy plane (blue), and magnetic field lines outside the droplet are projected on the xz and yz plane (red). The angle θ is determined by the droplet major axis and the x axis.

B. External magnetic fields applied in a direction different from one of the flow main directions

1. Droplet shape and magnetization

We now take $\mathbf{H}_0 = (\hat{e}_x + \hat{e}_y)/\sqrt{2}$, so that the external magnetic field is perpendicular to the z axis and parallel to the $x = y$ plane. With this configuration, the droplet does not achieve a steady shape at $Ca = 0.12$ and $Ca_{\text{mag}} \geq 2$, at $Ca = 0.1$ and $Ca_{\text{mag}} \geq 6$, and at $Ca = 0.08$ and $Ca_{\text{mag}} \geq 16$. We explore the parameter space accordingly.

Figure 13 shows a three-dimensional view of the droplet at $Ca = 0.02$ and $Ca_{\text{mag}} = 20$. Even though symmetric with respect to the xy plane, the prolatelike droplet is not symmetric with respect to the x and y axis separately. The droplet distortion is now measured with Taylor's parameter $D = (L - B)/(L + B)$, where L and B are, respectively, the droplet major semiaxis (half length) and minor semiaxis (half breadth) in the xy plane [31,32]. The droplet orientation is measured with the angle θ between the droplet major axis and the x axis, where $\theta = 0$ is the direction of flow extension and $\theta = \pi/4$ is the direction of the external field. Figure 14 shows how D and θ (normalized by $\pi/4$) vary with Ca_{mag} and Ca . Viscous and magnetic forces stretch the droplet

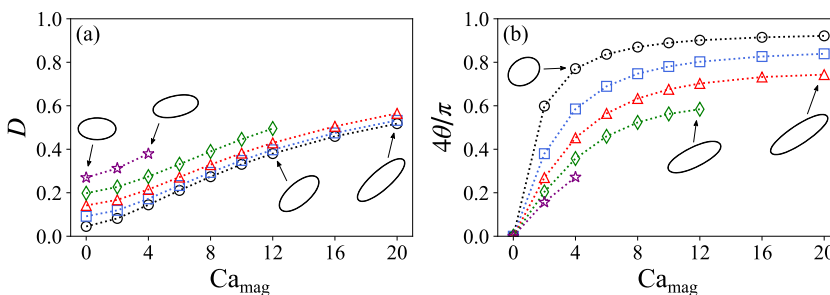


FIG. 14. (a) Droplet distortion (D) and (b) orientation (θ , measured with respect to the x axis and normalized by $\pi/4$) as a function of Ca_{mag} when the external magnetic field is applied in the $x = y$ direction. The results are for $Ca = 0.02$ (black circles), $Ca = 0.04$ (blue squares), $Ca = 0.06$ (red triangles), $Ca = 0.08$ (green diamonds), and $Ca = 0.1$ (magenta stars). The insets show the droplet cross section in the xy plane at different conditions.

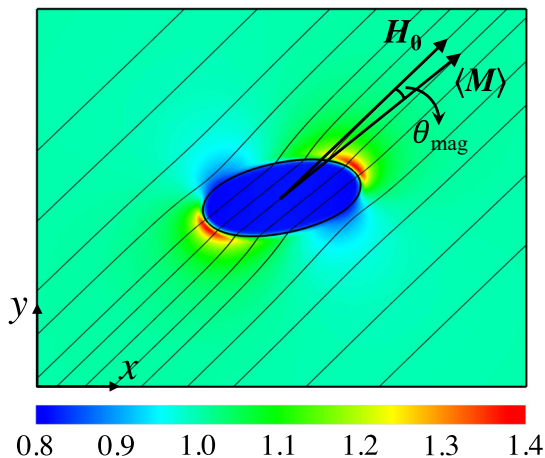


FIG. 15. Magnitude of the magnetic field and magnetic field lines in the xy plane. The result is for $Ca = 0.1$ when the external magnetic field is applied in the $x = y$ direction at $Ca_{\text{mag}} = 4$. The arrows (not to scale) indicate the direction of the external field \mathbf{H}_0 and the direction of the system magnetization $\langle \mathbf{M} \rangle = \beta \mathbf{M}$; θ_{mag} is the angle between them.

in directions that are not perpendicular to one another. The former is responsible for flow-induced extension in the x direction, whereas the latter is responsible for field-induced extension in the $x = y$ direction. The magnetic force can be generally split into three components: one that collaborates with viscous extension in the x direction, one that counteracts viscous compression in the y direction, and one that collaborates with viscous compression in the z direction. It follows that D grows with both Ca_{mag} and Ca [Fig. 14(a)]. The balance between viscous and magnetic forces also determines the droplet orientation in the flow. While the former tends to align the droplet with the direction of flow extension, the latter tends to align the droplet with the external field direction. At fixed Ca_{mag} , θ decreases as Ca increases; conversely, at fixed Ca , θ increases as Ca_{mag} increases. Hence, θ grows with Ca_{mag} and the curves of θ vs Ca_{mag} shift upwards as Ca falls [Fig. 14(b)]. The droplet orientation is $0 < \theta < \pi/4$; we expect $\theta = 0$ as $Ca_{\text{mag}}/Ca \rightarrow 0$ (or in the absence of external field) and $\theta = \pi/4$ as $Ca_{\text{mag}}/Ca \rightarrow \infty$ (or in the absence of external flow). The predictions also suggest that the dependence of D on Ca and of θ on Ca_{mag} becomes weaker as Ca_{mag} grows stronger. That is, there is a threshold value of Ca_{mag} above which a further increase in Ca_{mag} changes D without changing θ , which becomes a function of Ca only.

Figure 15 shows the magnetic field intensity and lines near the droplet in the xy plane at $Ca = 0.1$ and $Ca_{\text{mag}} = 4$ (see Fig. 8 for comparison). The magnetic field inside the droplet is uniform because the droplet is ellipsoidal, but the field lines are no longer parallel to the external field direction. Note that the regions of higher/lower field intensity outside the droplet and close to the interface are not symmetric with respect to the droplet main axes, deviating slightly from the regions of maximum/minimum curvature at the droplet tips. As a result, the magnetic force, which is always normal to the interface, induces a torque that tends to lean the droplet counterclockwise around the z axis (towards the external field direction). The droplet magnetization is locally aligned with the magnetic field inside the droplet because the ferrofluid is superparamagnetic. Therefore, the primary action of the magnetic torque is to align the droplet magnetization with the external field direction. Previous studies showed that superparamagnetic droplets also experience magnetic torques in simple shear flows under uniform magnetic fields [35,38]. In shear, however, the droplet orientation is inherently affected by the flow vorticity; here, in contrast, the planar extensional flow is vorticity-free by construction. The droplet tilts in the extensional flow only because the external field is not aligned with one of the flow main directions. As soon as magnetic forces stretch the

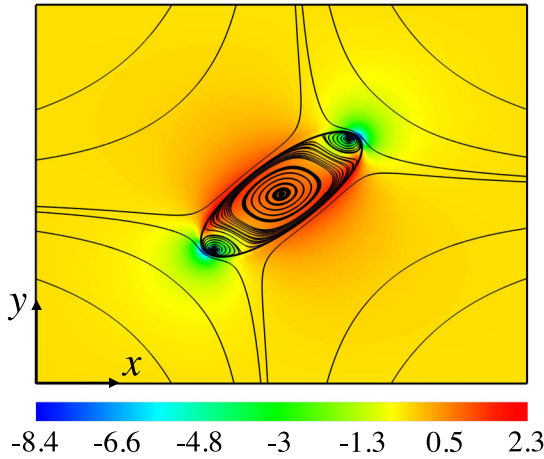


FIG. 16. z component of the flow vorticity ($\xi = \nabla \times \mathbf{u}$) and flow streamlines in the xy plane. The result is for $Ca = 0.04$ when the external magnetic field is applied in the $x = y$ direction at $Ca_{\text{mag}} = 16$.

droplet in the external field direction, viscous forces tend to tilt the droplet major axis clockwise around the z axis (towards the direction of flow extension); this creates an angle θ_{mag} between the droplet magnetization \mathbf{M} and the external field \mathbf{H}_0 (see Fig. 15), which leads to a magnetic torque at the droplet level. At the steady state, viscous and magnetic torques balance one another and the droplet orientation becomes stationary.

Figure 16 shows the z component of the flow vorticity and flow streamlines near the droplet in the xy plane at $Ca = 0.04$ and $Ca_{\text{mag}} = 16$ (see Fig. 7 for comparison). The competition between viscous and magnetic forces in directions that are not perpendicular to one another pushes the two vortices of negative vorticity toward the droplet tips and eventually merges the two vortices of positive vorticity into a large vortex around the droplet center. The flow inside the droplet becomes characterized by three recirculation regions, highlighting an intriguing field-induced topological transformation of the flow pattern at the droplet scale.

Macroscopically, the ferrofluid emulsion no longer responds as a superparamagnetic material, as there is a small angle θ_{mag} between the system magnetization $\langle \mathbf{M} \rangle = \beta \mathbf{M}$ and the external field \mathbf{H}_0 (see Fig. 15). Conversely, the bulk emulsion experiences a field-induced internal torque $\tau_{\text{mag}} = (Ca_{\text{mag}}/Ca) \langle \mathbf{M} \rangle \times \mathbf{H}_0$ whose intensity is $\tau_{\text{mag}} = (Ca_{\text{mag}}/Ca) \beta M \sin \theta_{\text{mag}}$. Figure 17 shows M as a function of Ca_{mag} and θ_{mag} as a function of Ca . Increasing the external field intensity stretches and tilts the droplet towards the external field direction (see Fig. 14). Both effects decrease the droplet demagnetizing factor, so that M grows with Ca_{mag} [Fig. 17(a)]. Increasing the strength of viscous forces also stretches the droplet, but hinders the droplet alignment with the external field direction (see Fig. 14). It turns out that the combined action of these two effects is not consequential to the droplet demagnetizing factor, so that M is nearly constant with Ca [Fig. 17(a)]. Additionally, θ_{mag} increases close to linearly with Ca and is a weak function of Ca_{mag} [Fig. 17(b)]. This suggests that the flow is the main responsible for promoting field-induced internal torques in the bulk emulsion, provided that an external magnetic field exists to trigger the droplet magnetization, as previously observed in simple shear flows [35,38]. Figure 18 shows that τ_{mag} (normalized by β) increases with Ca_{mag} and is approximately independent of Ca . The rationale is the following: first, τ_{mag} scales with Ca_{mag} , and increasing Ca_{mag} increases M without changing θ_{mag} ; second, even though τ_{mag} scales with $1/Ca$, increasing Ca increases θ_{mag} without changing M . Because θ_{mag} is generally small, so that $\sin \theta_{\text{mag}} \approx \theta_{\text{mag}}$, the net effects of changing Ca on τ_{mag} are negligible. In summary, the ferrofluid emulsion behaves like a bulk material that, when subjected to external magnetic fields, responds to external extensional loads with field-induced internal torques. This odd behavior is a characteristic

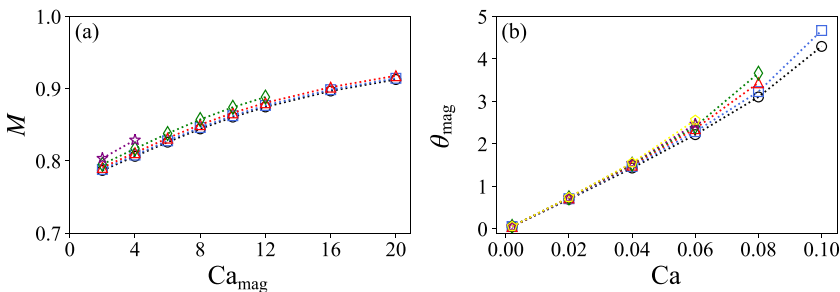


FIG. 17. (a) Magnitude of the droplet magnetization (M) as a function of Ca_{mag} . The results are for $Ca = 0.02$ (black circles), $Ca = 0.04$ (blue squares), $Ca = 0.06$ (red triangles), $Ca = 0.08$ (green diamonds), and $Ca = 0.1$ (magenta stars). (b) Angle between the ferrofluid emulsion bulk magnetization and the external field direction (θ_{mag} , in degrees) as a function of Ca . The results are for $Ca_{\text{mag}} = 2$ (black circles), $Ca_{\text{mag}} = 4$ (blue squares), $Ca_{\text{mag}} = 8$ (red triangles), $Ca_{\text{mag}} = 12$ (green diamonds), $Ca_{\text{mag}} = 16$ (magenta stars), and $Ca_{\text{mag}} = 20$ (yellow pentagons). In both cases, the external magnetic field is applied in the $x = y$ direction.

of chiral fluids, a new class of complex systems that has received increasing attention in recent years [75–78].

2. Emulsion rheology

Moving to rheology, Fig. 19 shows η_p and η_2 as a function of Ca_{mag} for different values of Ca . The trends are qualitatively similar to those discussed for Figs. 10 and 11. Because the droplet orientation is $0 < \theta < \pi/4$ [see Fig. 14(b)], the projection of the droplet major axis on the x axis is larger than the projection on the y axis. The viscous-hardening behavior of η_p in Fig. 19(a) is thus equivalent to that when the external field is in the x direction [see Fig. 10(a)], but η_p is now generally lower because of the mismatch between the primary directions of viscous and magnetic forces acting at the droplet surface. The same idea applies to the viscous-hardening behavior of η_2 in Fig. 19(b), which essentially is a less pronounced version of the results with the external field in the y direction [see Fig. 11(b)].

The steady-state rheology of complex fluids relies on a set of material functions that can capture the deviatoric part of the stress tensor in a motion with constant stretch history. The emergence of

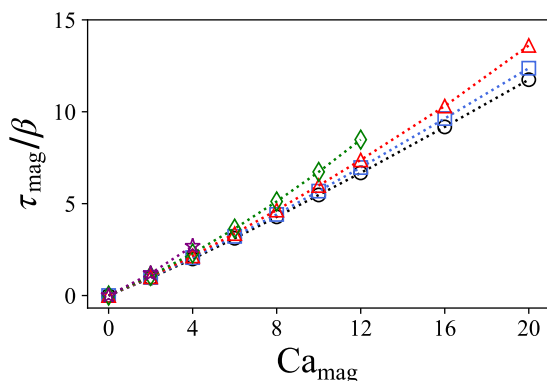


FIG. 18. Magnitude of the field-induced internal torque in the ferrofluid emulsion (τ_{mag}) as a function of Ca_{mag} when the external magnetic field is applied in the $x = y$ direction. The results are for $Ca = 0.02$ (black circles), $Ca = 0.04$ (blue squares), $Ca = 0.06$ (red triangles), $Ca = 0.08$ (green diamonds), and $Ca = 0.1$ (magenta stars). Note that τ_{mag} is normalized by the droplet volume fraction (β).

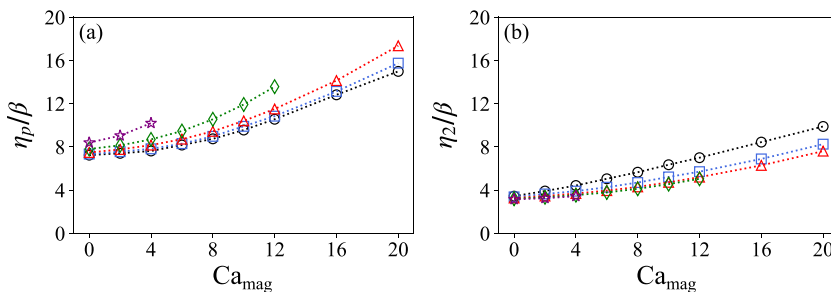


FIG. 19. Droplet contribution to the (a) planar extensional viscosity (η_p) and (b) second extensional viscosity (η_2) of the ferrofluid emulsion as a function of Ca_{mag} when the external magnetic field is applied in the $x = y$ direction. The results are for $Ca = 0.02$ (black circles), $Ca = 0.04$ (blue squares), $Ca = 0.06$ (red triangles), $Ca = 0.08$ (green diamonds), and $Ca = 0.1$ (magenta stars). Note that both η_p and η_2 are normalized by the droplet volume fraction (β).

field-induced internal torques in the system indicates that the droplet stress is no longer symmetric and contributes with shear stresses to the bulk stress tensor of the ferrofluid emulsion. As the two usual extensional viscosity coefficients are associated with normal stresses only, we must introduce new material functions to account for these unexpected shear stresses and fully characterize the stress state in planar extension. The parallel with shear rheology is straightforward: even though the rate-of-strain tensor has shear components only in viscometric flows, one still defines viscometric material functions associated with normal stresses. It is important to make a distinction between extensional motion and extensional loading at this point. The existence of shear stresses in extensional flows is related to the anisotropic nature of the fluid microstructure. Shear stresses appear as a macroscopic response to sustain the imposed extensional motion when the microstructure orientation is not aligned with one of the flow main directions. Here the microstructure of the ferrofluid emulsion consists of ferrofluid droplets whose intrinsic orientation is affected by the external field configuration. Additionally, it is instructive to revisit the definition of the droplet stress in Eq. (8). Because the droplet is now tilted with respect to the references axes, changes in the sign of the shear components of $\mathbf{x}\hat{\mathbf{n}}$ at the interface are not exactly antisymmetric; likewise, the distributions of κ and $\|\mathbf{H}\|^2$ at the interface are not exactly symmetric (see Fig. 15). As a result, the shear components of the integrals of $\kappa\mathbf{x}\hat{\mathbf{n}}$ and $\|\mathbf{H}\|^2\mathbf{x}\hat{\mathbf{n}}$ over S do not vanish; instead, they lead to nonsymmetric shear stresses in $\boldsymbol{\sigma}^d$.

Let \mathbf{S}^d and \mathbf{W}^d be the symmetric and skew-symmetric parts of $\boldsymbol{\sigma}^d$, respectively. We now define $\eta_s = S_{xy}^d$ and $\eta_r = W_{xy}^d$ as the dimensionless droplet contribution to the shear and rotational viscosity coefficients of ferrofluid emulsions in planar extension, respectively (see footnote 1). Note that η_s and η_r are new material functions associated with shear stresses in the xy plane of the planar extensional flow. Figure 20 shows η_s and η_r as a function of Ca_{mag} for different values of Ca . Because the shear stresses in the bulk emulsion are in the clockwise direction (see Figs. 15 and 16), σ_{yx}^d is positive and σ_{xy}^d is negative. To explain this further, we analyze the traction and compression terms of the droplet stress separately [see Eqs. (9) and (10)]. The traction contributions to σ_{xy}^d and σ_{yx}^d are both positive because the regions of high/low curvature at the interface coincide with those where the shear components of $\mathbf{x}\hat{\mathbf{n}}$ are positive/negative. However, these contributions are equal to one another because the curvature distribution is symmetric with respect to the droplet major axis. Following the same rationale, the compression contributions to σ_{xy}^d and σ_{yx}^d are both negative because the magnetic field intensity near the droplet is higher/lower near the regions where the shear components of $\mathbf{x}\hat{\mathbf{n}}$ are positive/negative. Nevertheless, the distribution of magnetic field intensity near the interface is not symmetric with respect to the droplet major axis. The regions of high field intensity are dislocated in the counterclockwise direction from the droplet tips towards the regions where the xy component of $\mathbf{x}\hat{\mathbf{n}}$ is positive. Moreover, as the droplet orientation is $0 < \theta < \pi/4$

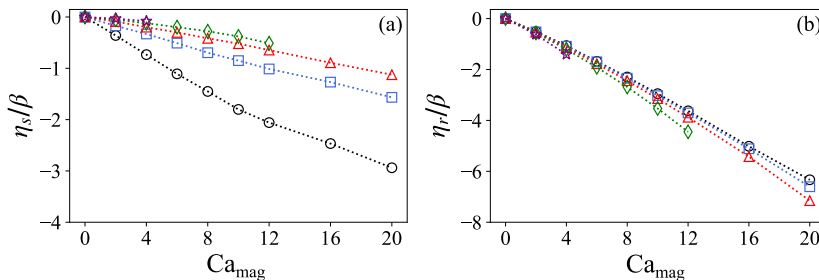


FIG. 20. Droplet contribution to the (a) shear viscosity (η_s) and (b) rotational viscosity (η_r) of the ferrofluid emulsion as a function of Ca_{mag} when the external magnetic field is applied in the $x = y$ direction. The results are for $Ca = 0.02$ (black circles), $Ca = 0.04$ (blue squares), $Ca = 0.06$ (red triangles), $Ca = 0.08$ (green diamonds), and $Ca = 0.1$ (magenta stars). Note that both η_s and η_r are normalized by the droplet volume fraction (β).

[see Fig. 14(b)], the xy component of $\mathbf{x}\hat{\mathbf{n}}$ is positive over a larger portion of the interface. The compression contribution to σ_{xy}^d is thus more intense than that associated with σ_{yx}^d . As a result, η_s is negative; based on the role Ca_{mag} and Ca play in the droplet distortion and orientation in the flow (see Fig. 14), it follows that η_s falls with Ca_{mag} and grows with Ca [Fig. 20(a)]. The rotational viscosity is strictly associated with the field-induced internal torque (see Fig. 18), so that η_r simply scales with τ_{mag} [Fig. 20(b)]. The fact that η_r is negative just reflects that the droplet contribution to the macroscopic flow opposes the magnetic torque induced at the droplet surface.

For the sake of completeness, we want to address the scenario where the external field configuration relative to the flow is arbitrary. In the more general case, the external field can entirely break the droplet symmetry, and so the resulting field-induced internal torque in the bulk emulsion can have any direction. Following the analysis presented here, this would lead to a nonsymmetric droplet stress fully populated with all six shear components, which would require eight material functions to fully characterize the stress state in planar extension: the two usual extensional viscosity coefficients associated with the normal stresses in each direction and three pairs of shear and rotational viscosity coefficients associated with the shear stresses in each plane. We anticipate that highly anisotropic microscopic states like this can also happen in other macroscopic motions such as simple shear, uniaxial extension, biaxial extension, etc. Therefore, a complete description of the rheology of ferrofluid emulsions will often require the introduction of additional material functions to fully characterize the stress state. Remarkably, the activation of rotational degrees of freedom of superparamagnetic droplets with static magnetic fields is possible only in hydrodynamic flows, shedding light on the potential of ferrofluid emulsions as a new model system for chiral fluids with rich rheology and tunable properties [75–78].

V. CONCLUDING REMARKS

We presented a computational study of the dynamics of superparamagnetic ferrofluid droplets in planar extensional flows under the external action of uniform magnetic fields. For the sake of simplicity, we neglected both buoyancy and inertial effects, considered the case where the two liquid phases have the same viscosity, and assumed that the ferrofluid phase has a constant magnetic susceptibility. Using the particle stress of Cunha *et al.* [35], we also studied the effects of the external field configuration on the planar extensional rheology of dilute ferrofluid emulsions when the two-phase system is taken as a homogeneous material from a continuum perspective. Overall, we found that the droplet shape and magnetization are strongly coupled and result from the balance between viscous, magnetic, and capillary forces at the droplet surface, which depends on the external field intensity and direction relative to the flow. Importantly, the droplet shape and magnetization

at the microscopic level dictate the rheological response of the resulting ferrofluid emulsion at the macroscopic level.

When the external magnetic field is applied in one of the flow main directions (extension, compression, or neutral), the droplet assumes the shape of a general ellipsoid whose main axes are aligned with the reference axes. The external field configuration can be adjusted to control the droplet deformation, induce or prevent droplet breakup, and change the droplet shape from prolatelike to oblate. The vorticity field is symmetric, the flow inside the droplet is characterized by four recirculation regions, and the ferrofluid emulsion responds as a superparamagnetic material for which the bulk magnetization is aligned with the external field direction and the effective susceptibility varies with the droplet response. Moreover, the droplet contribution to the two extensional viscosity coefficients associated with the normal stresses of the bulk emulsion either remains constant or increases with the external field intensity (field-induced viscous-hardening). The only exception occurs when the external field is applied in the flow neutral direction, where increasing the external field intensity keeps the planar extensional viscosity constant and decreases the second extensional viscosity (field-induced viscous softening). In parallel with suspensions of pusher bacteria [74], the predictions suggest that the droplet can eventually facilitate part of the imposed motion with negative contributions to the second extensional viscosity. In general, the response of ferrofluid emulsions in planar extensional flows is very different from that previously observed in viscometric flows such as simple shear [35,36].

Conversely, the droplet tilts in the extensional flow when the external magnetic field is applied in a direction that does not coincide with one of the flow main directions. The ferrofluid emulsion no longer responds as a superparamagnetic material, the vorticity field is no longer symmetric, and the flow inside the droplet becomes characterized by three recirculation regions, highlighting a dramatic field-induced topological transformation of the flow at the droplet level. Similar to what happens in shear flows, the system experiences a field-induced internal torque because the droplet magnetization is no longer aligned with the external field direction [35,38]. Because of this highly anisotropic microstructure, the ferrofluid emulsion develops nonsymmetric shear stresses to sustain the imposed extensional motion and displays novel rheological signatures that can be captured only with the introduction of appropriate material functions to fully characterize the stress state. The field-induced activation and control of rotational degrees of freedom of superparamagnetic droplets in hydrodynamic flows throw light on ferrofluid emulsions as a new model system for chiral fluids with rich rheology and transformational properties [75–78].

The data that support the findings of this study are available from the corresponding author upon reasonable request.

ACKNOWLEDGMENTS

This research was supported by CNPq (Ministry of Science, Technology, and Innovation of Brazil) under grants 131422/2021-9 (A.L.G.), 304095/2018-4 (R.L.T.), and 310631/2021-1 (T.F.O.).

APPENDIX A

1. Numerical methodology

a. Projection method for the hydrodynamic problem

The mass conservation and momentum balance equations of the two-phase flow are solved with the projection method of Kim and Moin [79]. Starting from the velocity \mathbf{u}^n at the present time step, the method introduces a fractional step for a tentative velocity \mathbf{u}^* and a tentative pressure P^* ; the former is then projected onto the divergence-free space to determine the true velocity \mathbf{u}^{n+1} and the true pressure P^{n+1} at the next time step. After the incompressibility constraint, the fractional step

consists of

$$\rho \left(\frac{\mathbf{u}^* - \mathbf{u}^n}{\Delta t} \right) = -\rho(\mathbf{u} \cdot \nabla \mathbf{u})^{n+\frac{1}{2}} + \frac{\eta}{2} \nabla^2 (\mathbf{u}^n + \mathbf{u}^*) + \mathbf{F}_c^{n+\frac{1}{2}} + \mathbf{F}_m^{n+\frac{1}{2}} \quad (\text{A1})$$

and

$$\nabla^2 P^* = \frac{\rho}{\Delta t} \nabla \cdot \mathbf{u}^*, \quad (\text{A2})$$

where the terms at $n + 1/2$ are extrapolated with a second-order Adams-Bashforth scheme.

Equations (A1) and (A2) are discretized using second-order finite differences in a staggered grid; the only exception is for the advective term, which is discretized using a second-order essentially nonoscillatory (ENO) formula, combined with upwind scheme. The linear systems for \mathbf{u}^* and P^* are solved using a conjugate gradient algorithm with symmetric successive over-relaxation (SSOR) and multigrid preconditioning, respectively. The true velocity and the true pressure are then calculated as $\mathbf{u}^{n+1} = \mathbf{u}^* - (\Delta t/\rho)\nabla P^*$ and $P^{n+1} = P^* - [\eta\Delta t/(2\rho)]\nabla^2 P^*$.

b. Laplace equation for the magnetic problem

Equation (3) for the magnetic potential with $\zeta_\varepsilon(\phi)$ instead of $\zeta(\mathbf{x})$ is discretized using centered, second-order finite differences, and the linear system for ψ is solved using a conjugate gradient algorithm with multigrid preconditioning. This is the same numerical scheme used to solve for the tentative pressure in the projection method.

c. Level set method for the interfacial problem

The fluid interface that defines the droplet surface is captured with the level method, as detailed by Osher and Fedkiw [60] and reviewed by Sethian and Smereka [61] and Gibou *et al.* [62]. The method couples the traditional equation for the advection of the level set function in the flow,

$$\frac{\partial \phi}{\partial t} + \mathbf{u} \cdot \nabla \phi = 0, \quad (\text{A3})$$

with an additional transport equation for its reinitialization,

$$\frac{\partial \phi}{\partial \tau} + S(\phi)(\|\nabla \phi\| - 1) - \Upsilon \delta(\phi)\|\nabla \phi\| = 0, \quad (\text{A4})$$

where τ is an artificial time, Υ is a correction to ensure volume conservation, and $S(\phi)$ is the signal function; the correction terms is

$$\Upsilon = \frac{\int_{\Omega} \delta(\phi)[S(\phi)(\|\nabla \phi\| - 1)] dV}{\int_{\Omega} \delta^2(\phi)\|\nabla \phi\| dV}, \quad (\text{A5})$$

where Ω is an individual grid cell, and the signal function is

$$S(\phi) = \frac{\phi}{\sqrt{\phi^2 + \|\nabla \phi\|^2 \Delta x^2}}. \quad (\text{A6})$$

Equations (A3) and (A4) are solved with a conservative Gudonov's method in which the spatial derivatives are discretized using a fifth-order weighted essentially nonoscillatory (WENO) scheme and time is integrated using a third-order strong stability preserving (SSP) Runge-Kutta scheme. Surface integrals of an arbitrary function $\mathfrak{F}(\mathbf{x}, t)$ over the droplet surface S are transformed into volume integrals over the total volume V of the system as

$$\int_S \mathfrak{F} dS = \int_V \mathfrak{F} \delta_\varepsilon(\phi)\|\nabla \phi\| dV \quad (\text{A7})$$

and calculated using a second-order quadrature in a 27-point cubic stencil.

TABLE I. Mesh convergence study in terms of the droplet distortion in the xy plane (D_{xy}), the droplet magnetization (M , normalized by β), and the xx component of the traction and compression terms of the particle stress ($\sigma_{t,xx}^d$ and $\sigma_{c,xx}^d$, both normalized by β). The results are for $Ca = 0.02$ and $Ca_{\text{mag}} = 20$ when the external magnetic field is applied in the x direction.

Mesh	Grid cells	Meshing size	D_{xy}	$\sigma_{t,xx}^d/\beta$	$\sigma_{c,xx}^d/\beta$	M/β
M1	829 440	0.1042	0.5703	0.7723	-2.2728	0.004171
M2	1 966 080	0.0781	0.5765	0.7817	-2.2673	0.004151
M3	3 840 000	0.0625	0.5804	0.7869	-2.2649	0.004142
M4	6 635 520	0.0520	0.5835	0.7906	-2.2629	0.004138

d. Computational mesh and convergence study

We performed a mesh convergence study to verify the accuracy of the numerical solutions for a representative case where $Ca = 0.02$, $Ca_{\text{mag}} = 20$, and the external magnetic field is applied in the x direction. We tested four different regular meshes (termed M1 to M4) for which the number of cells along the longest side of the flow domain is set to 120, 160, 200, and 240, respectively; therefore, the total number of grid cells and the meshing size vary from $\sim 800\,000$ to $\sim 6\,600\,000$ and from ~ 0.1 to ~ 0.05 , respectively. In all cases, the time step is set to $\Delta t \approx 0.25\Delta x/\|\mathbf{u}_{\text{max}}\|$, where $\|\mathbf{u}_{\text{max}}\| \approx 8$ is the maximum flow velocity, as determined by the essential boundary condition and the domain size.

Table I summarizes the steady-state results for the droplet distortion in the xy plane, D_{xy} , the droplet magnetization, M , and the xx component of the traction and compression terms of the particle stress, $\sigma_{t,xx}^d$ and $\sigma_{c,xx}^d$, respectively. As the refinement increases from mesh M1 to mesh M4, the results change in less than $\sim 1.2\%$, $\sim 0.7\%$, and $\sim 0.5\%$, respectively, demonstrating that the hydrodynamic, magnetic, and level set variables indeed converge with the spatial discretization. All simulations presented in the main paper were computed with mesh M3 and $\Delta t = 0.002$.

APPENDIX B

Here we derive the expression for the particle stress of ferrofluids droplets in suspension (see Sec. II to review the model assumptions). We start with the capillary and magnetic forces at the droplet surface written as $\mathbf{F}_c = -\sigma\kappa\delta(\phi)\hat{\mathbf{n}}$ and $\mathbf{F}_m = \mu_0(\zeta(\phi) - 1)\mathbf{H} \cdot \nabla\mathbf{H}$, respectively. Note that the latter is equivalent to

$$\mathbf{F}_m = \nabla \left[\frac{1}{2}\mu_0(\zeta(\phi) - 1)\|\mathbf{H}\|^2 \right] - \frac{1}{2}\mu_0\|\mathbf{H}\|^2\nabla\zeta(\phi). \quad (\text{B1})$$

While the first term of Eq. (B1) can be readily incorporated into a modified pressure field, thus playing no role in the flow other than ensuring incompressibility, the second is of special importance for the droplet dynamics and emulsion rheology. As $\nabla\zeta(\phi) = -\chi\delta(\phi)\hat{\mathbf{n}}$, where we have used that $\nabla\zeta(\phi) = -\chi\nabla\mathcal{H}(\phi)$, $\nabla\mathcal{H}(\phi) = \delta(\phi)\nabla\phi$, and $\hat{\mathbf{n}} = \nabla\phi$, the second term of Eq. (B1) corresponds to a normal stress jump of intensity $\frac{1}{2}\mu_0\chi\|\mathbf{H}\|^2$ across the fluid interface.

To formally demonstrate the stress jump across the interface, we take a control volume of width $2e$ around a portion Γ of the droplet surface, as illustrated in Fig. 21. The integral momentum balance reads

$$(\hat{\mathbf{n}} \cdot \boldsymbol{\sigma}^o)\Gamma^o - (\hat{\mathbf{n}} \cdot \boldsymbol{\sigma}^i)\Gamma^i + \int_{-e}^e \left[\frac{1}{2}\mu_0\chi\|\mathbf{H}\|^2 - \sigma\kappa \right] \Gamma\delta(\phi)\hat{\mathbf{n}} d\phi = \mathbf{0}, \quad (\text{B2})$$

where $\boldsymbol{\sigma}$ is the bulk stress tensor of each fluid phase and the superscripts i and o are used to distinguish quantities of the inner and outer phases, respectively. Using the convolution property

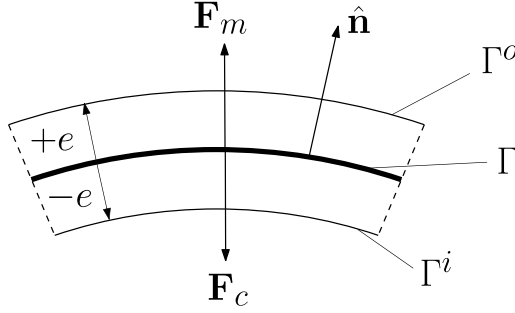


FIG. 21. Force balance in a control volume of width $2e$ around a portion Γ of the droplet surface. The superscripts i and o distinguish the inner and the outer phases, respectively.

of $\delta(\phi)$ and taking the limit $e \rightarrow 0$, Eq. (B2) becomes

$$\hat{\mathbf{n}} \cdot \boldsymbol{\sigma}^o - \hat{\mathbf{n}} \cdot \boldsymbol{\sigma}^i + \frac{1}{2} \mu_0 \chi \|\mathbf{H}\|^2 \hat{\mathbf{n}} - \sigma \kappa \hat{\mathbf{n}} = \mathbf{0}, \quad (\text{B3})$$

which is the same as

$$\Delta \mathbf{f} = \sigma \kappa \hat{\mathbf{n}} - \frac{1}{2} \mu_0 \chi \|\mathbf{H}\|^2 \hat{\mathbf{n}}, \quad (\text{B4})$$

where $\Delta \mathbf{f} = \hat{\mathbf{n}} \cdot [\boldsymbol{\sigma}^o - \boldsymbol{\sigma}^i]$ is the stress jump.

To determine the particle stress of ferrofluid droplets, we combine Eq. (B4) for the stress jump with the original formulation of Batchelor [44] for the particle stress of general particulate systems. This leads to

$$\boldsymbol{\sigma}^d = \frac{1}{V} \int_S \left[\sigma \kappa - \frac{1}{2} \mu_0 \chi \|\mathbf{H}\|^2 \right] \mathbf{x} \hat{\mathbf{n}} dS, \quad (\text{B5})$$

which is the dimensional counterpart of Eq. (8).

It is worth mentioning that this derivation is exact and does not depend on the interfacial thickness that the level set method uses to regularize the behavior of discontinuous properties across the interface.

-
- [1] R. E. Rosensweig, *Ferrohydrodynamics* (Cambridge University Press, New York, NY, 1985).
 - [2] S. Odenbach, *Ferrofluids: Magnetically Controllable Fluids and Their Applications* (Springer, Bremen, Germany, 2002).
 - [3] S. Odenbach, *Colloidal Magnetic Fluids: Basics, Development and Application of Ferrofluids* (Springer, Dresden, Germany, 2009).
 - [4] P. S. Stephen, Low viscosity magnetic fluid obtained by the colloidal suspension of magnetic particles, United States Patent and Trademark Office Granted Patent, Patent No: US3215572 (1965).
 - [5] R.-J. Yang, H.-H. Hou, Y.-N. Wang, and L.-M. Fu, Micro-magnetofluidics in microfluidic systems: A review, *Sens. Actuators B* **224**, 1 (2016).
 - [6] X. Zhang, L. Sun, Y. Yu, and Y. Zhao, Flexible ferrofluids: Design and applications, *Adv. Mater.* **31**, 1903497 (2019).
 - [7] E. Al-Hetlani and M. O. Amin, Continuous magnetic droplets and microfluidics: Generation, manipulation, synthesis and detection, *Microchim. Acta* **186**, 55 (2019).
 - [8] G.-P. Zhu, Q.-Y. Wang, Z.-K. Ma, S.-H. Wu, and Y.-P. Guo, Droplet manipulation under a magnetic field: A review, *Biosensors* **12**, 156 (2022).

- [9] M. Backholm, M. Vuckovac, J. Schreier, M. Latikka, M. Hummel, M. B. Linder, and R. H. A. Ras, Oscillating ferrofluid droplet microrheology of liquid-immersed sessile droplets, *Langmuir* **33**, 6300 (2017).
- [10] F. Serwane, A. Mongera, P. Rowghanian, D. A. Kealhofer, A. A. Lucio, Z. M. Hockenbery, and O. Campàs, *In vivo* quantification of spatially varying mechanical properties in developing tissues, *Nat. Methods* **14**, 181 (2017).
- [11] M. Latikka, M. Backholm, A. Baidya, A. Ballesio, A. Serve, G. Beaune, J. V. I. Timonen, T. Pradeep, and R. H. A. Ras, Ferrofluid microdroplet splitting for population-based microfluidics and interfacial tensiometry, *Adv. Sci.* **7**, 2000359 (2020).
- [12] X. Fan, X. Dong, A. C. Karacakol, H. Xie, and M. Sitti, Reconfigurable multifunctional ferrofluid droplet robots, *Proc. Natl. Acad. Sci. USA* **117**, 27916 (2020).
- [13] X. Fan, M. Sun, L. Sun, and H. Xie, Ferrofluid droplets as liquid microrobots with multiple deformabilities, *Adv. Funct. Mater.* **30**, 2000138 (2020).
- [14] Y. Ji, C. Gan, Y. Dai, X. Bai, Z. Zhu, L. Song, L. Wang, H. Chen, J. Zhong, and L. Feng, Deformable ferrofluid microrobot with omnidirectional self-adaptive mobility, *J. Appl. Phys.* **131**, 064701 (2022).
- [15] I. Torres-Díaz and C. Rinaldi, Recent progress in ferrofluids research: Novel applications of magnetically controllable and tunable fluids, *Soft Matter* **10**, 8584 (2014).
- [16] A. Spatafora-Salazar, D. M. Lohmeyer, L. H. P. Cunha, K. Joshi, and S. L. Biswal, Hierarchical assemblies of superparamagnetic colloids in time-varying magnetic fields, *Soft Matter* **17**, 1120 (2021).
- [17] O. Oehlsen, S. I. Cervantes-Ramírez, P. Cervantes-Avilés, and I. A. Medina-Velo, Approaches on ferrofluid synthesis and applications: Current status and future perspectives, *ACS Omega* **7**, 3134 (2022).
- [18] C. Flament, S. Laci, J.-C. Bacri, A. Cebers, S. Neveu, and R. Perzynski, Measurements of ferrofluid surface tension in confined geometry, *Phys. Rev. E* **53**, 4801 (1996).
- [19] S. Banerjee, M. Fasnacht, S. Garoff, and M. Widom, Elongation of confined ferrofluid droplets under applied fields, *Phys. Rev. E* **60**, 4272 (1999).
- [20] S. Afkhami, Y. Renardy, M. Renardy, J. S. Riffle, and T. St. Pierre, Field-induced motion of ferrofluid droplets through immiscible viscous media, *J. Fluid Mech.* **610**, 363 (2008).
- [21] S. Afkhami, A. J. Tyler, Y. Renardy, M. Renardy, T. G. St. Pierre, R. C. Woodward, and J. S. Riffle, Deformation of a hydrophobic ferrofluid droplet suspended in a viscous medium under uniform magnetic fields, *J. Fluid Mech.* **663**, 358 (2010).
- [22] C.-Y. Chen, H.-C. Hsueh, S.-Y. Wang, and Y.-H. Li, Self-assembly and novel planetary motion of ferrofluid drops in a rotational magnetic field, *Microfluid. Nanofluid.* **18**, 795 (2015).
- [23] P. Rowghanian, C. D. Meinhardt, and O. Campàs, Dynamics of ferrofluid drop deformations under spatially uniform magnetic fields, *J. Fluid Mech.* **802**, 245 (2016).
- [24] S. Afkhami and Y. Renardy, Ferrofluids and magnetically guided superparamagnetic particles in flows: A review of simulations and modeling, *J. Eng. Math.* **107**, 231 (2017).
- [25] J. Erdmanis, G. Kitenbergs, R. Perzynski, and A. Cēbers, Magnetic micro-droplet in rotating field: Numerical simulation and comparison with experiment, *J. Fluid Mech.* **821**, 266 (2017).
- [26] M. Qiu, S. Afkhami, C.-Y. Chen, and J. J. Feng, Interaction of a pair of ferrofluid drops in a rotating magnetic field, *J. Fluid Mech.* **846**, 121 (2018).
- [27] K. Misra, Magnetic (electric) drop deformation in uniform external fields: Volume averaged methods and formation of static and dynamic conical tips, *Phys. Fluids* **32**, 107104 (2020).
- [28] A. P. Stikuts, R. Perzynski, and A. Cēbers, Small deformation theory for a magnetic droplet in a rotating field, *Phys. Fluids* **34**, 052010 (2022).
- [29] A. Langins, A. P. Stikuts, and A. Cēbers, A three-dimensional boundary element method algorithm for simulations of magnetic fluid droplet dynamics, *Phys. Fluids* **34**, 062105 (2022).
- [30] W. C. Jesus, A. M. Roma, and H. D. Ceniceros, Deformation of a sheared magnetic droplet in a viscous fluid, *Commun. Comput. Phys.* **24**, 332 (2018).
- [31] G. I. Taylor, The viscosity of a fluid containing small drops of another fluid, *Proc. R. Soc. A* **138**, 41 (1932).
- [32] G. I. Taylor, The formation of emulsions in definable fields of flow, *Proc. R. Soc. A* **146**, 501 (1934).

- [33] Md R. Hassan, J. Zhang, and C. Wang, Deformation of a ferrofluid droplet in simple shear flows under uniform magnetic fields, *Phys. Fluids* **30**, 092002 (2018).
- [34] P. Capobianchi, M. Lappa, and M. S. N. Oliveira, Deformation of a ferrofluid droplet in a simple shear flow under the effect of a constant magnetic field, *Comput. Fluids* **173**, 313 (2018).
- [35] L. H. P. Cunha, I. R. Siqueira, F. R. Cunha, and T. F. Oliveira, Effects of external magnetic fields on the rheology and magnetization of dilute emulsions of ferrofluid droplets in shear flows, *Phys. Fluids* **32**, 073306 (2020).
- [36] S. Ishida and D. Matsunaga, Rheology of a dilute ferrofluid droplet suspension in shear flow: Viscosity and normal stress differences, *Phys. Rev. Fluids* **5**, 123603 (2020).
- [37] P. Capobianchi, M. Lappa, M. S. N. Oliveira, and F. T. Pinho, Shear rheology of a dilute emulsion of ferrofluid droplets dispersed in a nonmagnetizable carrier fluid under the influence of a uniform magnetic field, *J. Rheol.* **65**, 925 (2021).
- [38] V. G. Abicalil, R. F. Abdo, L. H. P. Cunha, and T. F. Oliveira, On the magnetization of dilute ferrofluid emulsions in shear flows, *Phys. Fluids* **33**, 053313 (2021).
- [39] L. H. P. Cunha, I. R. Siqueira, T. F. Oliveira, and H. D. Ceniceros, Field-induced control of ferrofluid emulsion rheology and droplet break-up in shear flows, *Phys. Fluids* **30**, 122110 (2018).
- [40] M. R. Hassan and C. Wang, Magnetic field induced ferrofluid droplet breakup in a simple shear flow at a low Reynolds number, *Phys. Fluids* **31**, 127104 (2019).
- [41] M. Majidi, M. A. Bijarchi, A. G. Arani, M. H. Rahimian, and M. B. Shafii, Magnetic field-induced control of a compound ferrofluid droplet deformation and breakup in shear flow using a hybrid lattice Boltzmann-finite difference method, *Int. J. Multiphase Flow* **146**, 103846 (2022).
- [42] S. Ishida, Y. Yang, F. Meng, and D. Matsunaga, Field-controlling patterns of sheared ferrofluid droplets, *Phys. Fluids* **34**, 063309 (2022).
- [43] R. F. Abdo, V. G. Abicalil, L. H. P. Cunha, and T. F. Oliveira, On the rheology and magnetization of dilute magnetic emulsions under small amplitude oscillatory shear, *J. Fluid Mech.* **955**, A3 (2023).
- [44] G. K. Batchelor, The stress system in a suspension of force-free particles, *J. Fluid Mech.* **41**, 545 (1970).
- [45] S. Kim and S. J. Karrila, *Microhydrodynamics: Principles and Selected Applications* (Butterworth-Heinemann, Boston, MA, 1991).
- [46] D. Barthès-Biesel, *Microhydrodynamics and Complex Fluids* (CRC Press, Boca Raton, FL, 2012).
- [47] M. R. Kennedy, C. Pozrikidis, and R. Skalak, Motion and deformation of liquid drops, and the rheology of dilute emulsions in simple shear flow, *Comput. Fluids* **23**, 251 (1994).
- [48] X. Li and C. Pozrikidis, The effect of surfactants on drop deformation and on the rheology of dilute emulsions in Stokes flow, *J. Fluid Mech.* **341**, 165 (1997).
- [49] J. Bławdziewicz, P. Vlahovska, and M. Loewenberg, Rheology of a dilute emulsion of surfactant-covered spherical drops, *Physica A* **276**, 50 (2000).
- [50] P. Vlahovska, J. Bławdziewicz, and M. Loewenberg, Nonlinear rheology of a dilute emulsion of surfactant-covered spherical drops in time-dependent flows, *J. Fluid Mech.* **463**, 1 (2002).
- [51] S. Mandal, S. Das, and S. Chakraborty, Effect of Marangoni stress on the bulk rheology of a dilute emulsion of surfactant-laden deformable droplets in linear flows, *Phys. Rev. Fluids* **2**, 113604 (2017).
- [52] P. H. N. Pimenta and T. F. Oliveira, Study on the rheology of a dilute emulsion of surfactant-covered droplets using the level set and closest point methods, *Phys. Fluids* **33**, 103306 (2021).
- [53] R. I. Tanner, A test particle approach to flow classification for viscoelastic fluids, *AIChE J.* **22**, 910 (1976).
- [54] W. L. Olbricht, J. M. Rallison, and L. G. Leal, Strong flow criteria based on microstructure deformation, *J. Non-Newtonian Fluid Mech.* **10**, 291 (1982).
- [55] R. L. Thompson, Some perspectives on the dynamic history of a material element, *Int. J. Eng. Sci.* **46**, 224 (2008).
- [56] C. J. S. Petrie, Extensional viscosity: A critical discussion, *J. Non-Newtonian Fluid Mech.* **137**, 15 (2006).
- [57] C. J. S. Petrie, One hundred years of extensional flow, *J. Non-Newtonian Fluid Mech.* **137**, 1 (2006).
- [58] A. S. Hsu and L. G. Leal, Deformation of a viscoelastic drop in planar extensional flows of a Newtonian fluid, *J. Non-Newtonian Fluid Mech.* **160**, 176 (2009).
- [59] V. T. Hoang and J. M. Park, A Taylor analogy model for droplet dynamics in planar extensional flow, *Chem. Eng. Sci.* **204**, 27 (2019).

- [60] S. Osher and R. P. Fedkiw, *Level Set Methods and Dynamic Implicit Surfaces*, Applied Mathematical Sciences (Springer, New York, NY, 2005), Vol. 153.
- [61] J. A. Sethian and P. Smereka, Level set methods for fluid interfaces, *Annu. Rev. Fluid Mech.* **35**, 341 (2003).
- [62] F. Gibou, R. Fedkiw, and S. Osher, A review of level-set methods and some recent applications, *J. Comput. Phys.* **353**, 82 (2018).
- [63] C. Rinaldi and H. Brenner, Body versus surface forces in continuum mechanics: Is the Maxwell stress tensor a physically objective Cauchy stress? *Phys. Rev. E* **65**, 036615 (2002).
- [64] J. M. Rallison, A numerical study of the deformation and burst of a viscous drop in general shear flows, *J. Fluid Mech.* **109**, 465 (1981).
- [65] X. Liu, L. Li, J. Yu, G. Hao, W. Yu, and Y. Chen, Electric field mediated droplet spheroidizing in an extensional flow, *Phys. Fluids* **33**, 052116 (2021).
- [66] T. Zhu, R. Cheng, G. R. Sheppard, J. Locklin, and L. Mao, Magnetic-field-assisted fabrication and manipulation of nonspherical polymer particles in ferrofluid-based droplet microfluidics, *Langmuir* **31**, 8531 (2015).
- [67] S. Zhao, J.-Y. Zhang, Y. Fu, S. Zhu, H. C. Shum, X. Liu, Z. Wang, R. Ye, B. Z. Tang, T. P. Russell, and Y. Chai, Shape-reconfigurable ferrofluids, *Nano Lett.* **22**, 5538 (2022).
- [68] J. A. Osborn, Demagnetizing factors of the general ellipsoid, *Phys. Rev.* **67**, 351 (1945).
- [69] D. Takahashi and V. C. Oliveira Jr., Ellipsoids (v1. 0): 3-D magnetic modelling of ellipsoidal bodies, *Geosci. Model Develop.* **10**, 3591 (2017).
- [70] Yu. I. Dikanskĭ, A. R. Zakinyan, and N. Yu. Konstantinova, On the permeability of a magnetodielectric emulsion, *Tech. Phys.* **53**, 19 (2008).
- [71] A. O. Ivanov, O. B. Kuznetsova, and I. M. Subbotin, Magnetic properties of ferrofluid emulsions: Model of non-interacting droplets, *Magneto hydrodynamics* **47**, 129 (2011).
- [72] A. O. Ivanov, O. B. Kuznetsova, and I. M. Subbotin, Magnetic properties of ferrofluid emulsions: The effect of droplet elongation, *Magneto hydrodynamics* **49**, 287 (2013).
- [73] A. O. Ivanov and O. B. Kuznetsova, Nonmonotonic field-dependent magnetic permeability of a paramagnetic ferrofluid emulsion, *Phys. Rev. E* **85**, 041405 (2012).
- [74] D. Saintillan, Rheology of active fluids, *Annu. Rev. Fluid Mech.* **50**, 563 (2018).
- [75] V. Soni, E. S. Bililign, S. Magkiriadou, S. Sacanna, D. Bartolo, M. J. Shelley, and W. Irvine, The odd free surface flows of a colloidal chiral fluid, *Nat. Phys.* **15**, 1188 (2019).
- [76] T. A. Witten and H. Diamant, A review of shaped colloidal particles in fluids: Anisotropy and chirality, *Rep. Prog. Phys.* **83**, 116601 (2020).
- [77] M. Han, M. Fruchart, C. Scheibner, S. Vaikuntanathan, J. J. De Pablo, and V. Vitelli, Fluctuating hydrodynamics of chiral active fluids, *Nat. Phys.* **17**, 1260 (2021).
- [78] R. Lier, J. Armas, S. Bo, C. Duclut, F. Jülcher, and P. Surówka, Passive odd viscoelasticity, *Phys. Rev. E* **105**, 054607 (2022).
- [79] J. Kim and P. Moin, Application of a fractional-step method to incompressible Navier-Stokes equations, *J. Comput. Phys.* **59**, 308 (1985).